Biochem. J. (2015) **466**, 253–262 (Printed in Great Britain) doi:10.1042/BJ20141211

Catalytic surface radical in dye-decolorizing peroxidase: a computational, spectroscopic and site-directed mutagenesis study

Dolores Linde*, Rebecca Pogni†[1], Marina Cañellas‡§[1], Fátima Lucas‡, Victor Guallar‡‖, Maria Camilla Baratto†, Adalgisa Sinicropi†, Verónica Sáez-Jiménez*, Cristina Coscolín*, Antonio Romero*, Francisco Javier Medrano*, Francisco J. Ruiz-Dueñas*[2] and Angel T. Martínez*[2]

*Centro de Investigaciones Biológicas, CSIC, Ramiro de Maeztu 9, E-28040 Madrid, Spain
†Department of Biotechnology, Chemistry and Pharmacy, University of Siena, I-53100, Siena, Italy
‡Joint BSC-CRG-IRB Research Program in Computational Biology, Barcelona Supercomputing Center, Jordi Girona 29, E-08034 Barcelona, Spain
§Anaxomics Biotech, Balmes 89, E-08008 Barcelona, Spain
‖ICREA, Passeig Lluís Companys 23, E-08010 Barcelona, Spain

Dye-decolorizing peroxidase (DyP) of *Auricularia auricula-judae* has been expressed in *Escherichia coli* as a representative of a new DyP family, and subjected to mutagenic, spectroscopic, crystallographic and computational studies. The crystal structure of DyP shows a buried haem cofactor, and surface tryptophan and tyrosine residues potentially involved in long-range electron transfer from bulky dyes. Simulations using PELE (Protein Energy Landscape Exploration) software provided several binding-energy optima for the anthraquinone-type RB19 (Reactive Blue 19) near the above aromatic residues and the haem access-channel. Subsequent QM/MM (quantum mechanics/molecular mechanics) calculations showed a higher tendency of Trp-377 than other exposed haem-neighbouring residues to harbour a catalytic protein radical, and identified the electron-transfer pathway. The existence of such a radical in H_2O_2-activated DyP was shown by low-temperature EPR, being identified as a mixed tryptophanyl/tyrosyl radical in multifrequency experiments. The signal was dominated by the Trp-377 neutral radical contribution, which disappeared in the W377S variant, and included a tyrosyl contribution assigned to Tyr-337 after analysing the W377S spectra. Kinetics of substrate oxidation by DyP suggests the existence of high- and low-turnover sites. The high-turnover site for oxidation of RB19 ($k_{cat} > 200\ s^{-1}$) and other DyP substrates was assigned to Trp-377 since it was absent from the W377S variant. The low-turnover site/s (RB19 $k_{cat} \sim 20\ s^{-1}$) could correspond to the haem access-channel, since activity was decreased when the haem channel was occluded by the G169L mutation. If a tyrosine residue is also involved, it will be different from Tyr-337 since all activities are largely unaffected in the Y337S variant.

Key words: catalytic protein radical, dye-decolorizing peroxidase, EPR spectroscopy, molecular docking, QM/MM, site-directed mutagenesis.

INTRODUCTION

DyPs (dye-decolorizing peroxidases) (EC 1.11.1.19) represent a new family of haem peroxidases widespread in bacteria, archaea, fungi and other micro-organisms [1–4]. Among those of fungal origin, the enzymes from *Bjerkandera adusta* [5–7] and *Auricularia auricula-judae* [8–10] have been crystallized and biochemically characterized as representative DyPs from two phylogenetically different basidiomycetes (in orders Polyporales and Agaricales respectively). The structures of bacterial DyPs were simultaneously solved [11–15]. *B. adusta* DyP was largely characterized as a recombinant protein [16,17], whereas *A. auricula-judae* DyP was isolated from fungal cultures [18]. The latter enzyme has recently been overexpressed in *Escherichia coli* as inclusion bodies, and a refolding protocol was optimized yielding a recombinant DyP with basically the same properties as those of wild-type DyP [19].

Xenobiotic anthraquinone-type dyes are the best-known substrates for DyPs. Among wood-rotting basidiomycetes, DyP genes are significantly more frequent in the sequenced genomes of white-rot (ligninolytic) than brown-rot species [20]. This fact and their reported capability to degrade non-phenolic lignin model dimers, although with much lower efficiency than white-rot fungal LiPs (lignin peroxidases) [8], suggest a possible contribution of fungal DyPs to lignin biodegradation. Similarly, lignin-degrading capabilities have been claimed for bacterial DyPs [21,22].

Both lignin polymer and substituted anthraquinone dyes, such as RB19 (Reactive Blue 19) (Supplementary Figure S1A), cannot easily access the buried haem cofactor in DyPs and other haem peroxidases. As an alternative for oxidation of these bulky substrates, LRET (long-range electron transfer) from radical-forming aromatic residues at the DyP surface has been suggested [9,23]. Surface residues at the origin of LRET routes were first reported in *Phanerochaete chrysosporium* LiP [24] and *Pleurotus eryngii* VP (versatile peroxidase) [25], and later identified in the sequences of many putative LiPs and VPs from genomes of lignin-degrading white-rot basidiomycetes [20].

Abbreviations: ABTS, 2,2′-azinobis-(3-ethylbenzothiazoline-6-sulfonic acid); DMP, 2,6-dimethoxyphenol; DyP, dye-decolorizing peroxidase; hfcc, hyperfine coupling constant; LiP, lignin peroxidase; LRET, long-range electron transfer; MM, molecular mechanics; NBS, *N*-bromosuccinimide; PELE, Protein Energy Landscape Exploration; QM, quantum mechanics; RB5, Reactive Black 5; RB19, Reactive Blue 19; TNM, tetranitromethane; VA, veratryl alcohol; VP, versatile peroxidase; WT, wild-type.

[1] These authors contributed equally to this work.

[2] To whom correspondence should be addressed (email fjruiz@cib.csic.es and ATMartinez@cib.csic.es).

The co-ordinates and structure factors for Y147S, D168N, W377S, Y147S/W377S and Y147S/G169L/W377S mutant dye-decolorizing peroxidases from *Auricularia auricula-judae* have been deposited in the PDB under codes 4W7K, 4W7L, 4W7M, 4W7N and 4W7O respectively.

Computational analyses can help to explain these LRET processes, requiring, however, the combination of different levels of theory [26]. Long-timescale processes, such as substrate binding, can only be accomplished through MM (molecular mechanics) methods, whereas electron transfer requires QM (quantum mechanics)-based methods, such as QM/MM [27]. The combination of these techniques was shown to be a successful approach in the study of oxidation and electron-transfer processes in haem proteins [28].

In the present study, we expressed *A. auricula-judae* DyP in *E. coli*, solved the crystal structure of the recombinant enzyme and several site-directed variants, and used PELE (Protein Energy Landscape Exploration) [29] to describe the binding of its typical substrate RB19. Subsequent QM/MM analyses of binding sites indicate a preference for substrate oxidation at an exposed tryptophan residue, and identified the LRET pathway to haem. Simultaneously, a mixed tryptophanyl/tyrosyl radical was detected by EPR spectroscopy of the H_2O_2-activated WT (wild-type) DyP. A combined multifrequency EPR and computational approach, together with site-directed mutagenesis studies, enabled the identification of both protein radical contributions. Moreover, we associated a high-turnover site in DyP to the presence of a tryptophanyl radical, in agreement with the QM/MM predictions. In this way, a multidisciplinary evaluation of the role of protein radicals in DyP catalysis is provided.

MATERIALS AND METHODS

Chemicals

Among DyP substrates, RB19, DMP (2,6-dimethoxyphenol), RB5 (Reactive Black 5) and VA (veratryl alcohol) were from Sigma–Aldrich, and ABTS [2,2′-azinobis-(3-ethylbenzothiazoline-6-sulfonic acid)] was from Boehringer Mannheim (see Supplementary Figures S1A–S1E respectively and the Supplementary Methods for other chemicals).

DyP production, activation and purification

The DNA sequence coding mature DyP-I from *A. auricula-judae* (GenBank® accession number JQ650250) [18] was synthesized (ATG:biosynthetics), expressed in *E. coli*, activated *in vitro*, and purified as described in [19] (see the Supplementary Methods for details).

Site-directed mutagenesis and chemical modification of DyP

Simple DyP variants were produced by PCR using the pET23a-DyPI vector harbouring the mature protein-coding sequence of *A. auricula-judae* DyP as a template. For each mutation, direct and reverse primers were designed. For double (or triple) mutations, the mutated vector for the first (or second) mutation was used as template. The pET23a-DyPI plasmids containing the mutations were digested with endonuclease DpnI and transformed into *E. coli* DH5α cells for propagation.

Tryptophan and tyrosine residues in 3 μM WT DyP and the W377S variant were also chemically modified using up to 0.3 mM NBS (*N*-bromosuccinimide) and up to 40 mM TNM (tetranitromethane) (including 2.6 % ethanol) respectively [30]. Chemically modified enzymes were used for estimation of residual activity on RB19 (180 μM), DMP (7.5 mM), RB5 (15 μM) and ABTS (1.25 mM) (see the Supplementary Methods for PCR primers and conditions, and details on chemical modification).

Crystallization, data collection and refinement

Crystallization of WT DyP and five site-directed variants was optimized by the sitting-drop vapour-diffusion method. Crystals of WT DyP were obtained in 32.5 % PEG 4000, and those of all the variants were obtained in PEG 2000 MME (30–35 %). X-ray diffraction intensities were collected at the SOLEIL (Gyf-sur-Yvette, France) and ALBA (Barcelona, Spain) synchrotrons. The structure of WT DyP and its variants were solved by molecular replacement (see the Supplementary Methods for details; collection, refinement and final statistics are in Supplementary Table S1). Some of the structures did not show electron density for the first two or three residues at the N-terminus, but the whole sequence could be solved for two of them (PDB codes 4W7K and 4W7L). In contrast, the C-terminal region showed good electron density for all of the structures.

Enzyme kinetics

Steady-state kinetic constants were determined from absorbance increases during oxidation of DMP, ABTS and VA at pH 3 (pH 2.5 for VA) measured using a Thermo Spectronic UV–visible spectrophotometer. Absorbance decreases were followed for RB5 and RB19 oxidation (assayed at pH 3 and pH 3.5 respectively) using the same equipment. Eventual changes of enzyme molecular mass after turnover were investigated by MALDI–TOF (see the Supplementary Methods for details). Plotting and analysis of kinetic curves were carried out with SigmaPlot (version 11.0). Apparent affinity, turnover number and catalytic efficiency were estimated by non-linear least-squares fitting to the Michaelis–Menten model. The catalytic efficiency for VA was estimated by linear regression, since no saturation was attained. Calculation of two sets of kinetic constants was performed by adjusting to the Michaelis–Menten model the data from 0.2–10 μM RB19, 4–60 μM DMP, and 0.2–7 μM ABTS, separately from those of 50–270 μM RB19, 200–8000 μM DMP and 30–5000 μM ABTS.

Computational analyses: PELE, MD and QM/MM calculations

The starting structure (based on 4W7J) was prepared at pH 3.5, the optimal pH for RB19 oxidation, by adjusting the protonation state of ionizable residues. Histidine residues were double-protonated, except for His-304 (δ-protonated) and His-115 (ε-protonated), and several aspartic acids (residues 8, 12, 84, 129, 189, 246 and 270) and glutamic acids (residues 158, 220, 225 and 432) were kept in their acidic form. The RB19 atomic charges were derived from QM calculations (see the Supplementary Methods for details of system preparation). Then, RB19 was placed manually in 20 initial random positions on the protein surface and the protein–ligand conformational space was explored with PELE [29]. Results shown are based on 160 independent 48-h PELE simulations. Enhanced local sampling on Trp-377 was obtained with a 5 ns MD simulation allowing us to investigate the effect of solvent and charge fluctuations on the oxidative tendency of Trp-377 and RB19. QM/MM calculations were performed with QSite 5.7 (Schrödinger). Trp-377 LRET pathway calculations were performed with the QM/MM e-pathway approach [32] with His-304–Arg-311, Leu-323–Ala-325, Leu-373–Gln-375 and Asp-395 in the quantum region.

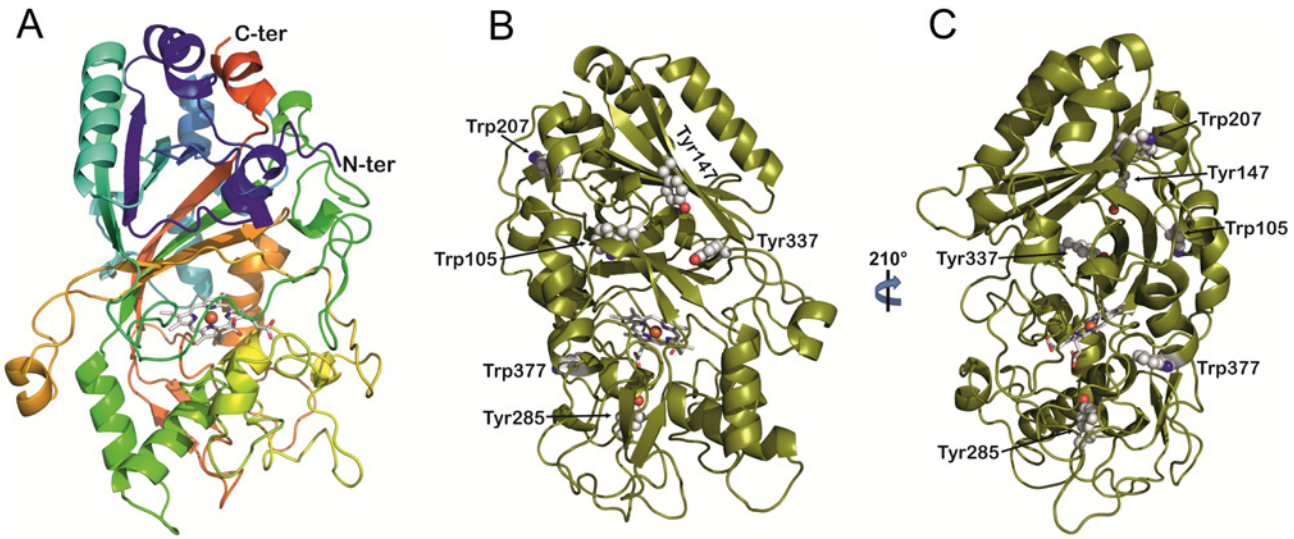

Figure 1 Folding of *A. auricula-judae* DyP and location of exposed aromatic residues

(**A**) General folding constituted by two domains, each of them including two large β-sheets and two or three helices, with the haem cofactor in the upper part of the lower domain [cartoon coloured from the N- to the C-terminus, with the haem shown as CPK (Corey–Pauling–Koltun) sticks]. (**B** and **C**) Location of exposed Trp-105, Tyr-147, Trp-207, Tyr-285, Tyr-337 and Trp-377 (as CPK spheres) in two different orientations of the DyP molecule (cartoon with the haem shown as CPK sticks). From PDB code 4W7J.

EPR spectroscopy and parameter calculations

CW (continuous wave) X-band (9.8 GHz) and W-band (94.17 GHz) experiments were recorded on Bruker Elexsys spectrometers E500 and E600 respectively (see the Supplementary Methods for details). DyP (0.1 μM) activation was carried out using an enzyme/H_2O_2 molar ratio of 1:10 in tartrate, pH 3. H_2O_2 addition was done directly in the EPR tube for the X-band measurements, and the reaction time before freezing was less than 10 s. For the W-band measurements, the H_2O_2 addition was done before filling the EPR tube resulting in a longer freezing time for the sample. Spectra simulations were performed by the Easyspin 4.5.5 package using the 'Pepper' function [33]. Preparatory force field calculations were performed before QM/MM estimation of EPR magnetic parameters. The QM/MM calculations were performed with the MOLCAS 7.4 package [34] coupled with a modified version of the MM package Tinker 4.2. EPR magnetic parameters - g-tensors, hfcc (hyperfine coupling constant) values and Mulliken spin densities - were computed via single-point calculations on the optimized structures using the ORCA2.9 package (F. Neese, University of Bonn, Bonn, Germany). Details of the protocols used to compute the EPR parameters are reported by Bernini et al. [36,37]

RESULTS AND DISCUSSION

Molecular structure: general fold and exposed aromatic residues

The crystal structure of *A. auricula-judae* WT DyP expressed in *E. coli* was solved at 1.79 Å (1 Å = 0.1 nm) resolution (PDB 4W7J), together with those of the Y147S, D168N, W377S, Y147S/W377S and Y147S/G169L/W377S variants (PDB codes 4W7K, 4W7L, 4W7M, 4W7N and 4W7O) solved at 1.05–1.40 Å resolution (Supplementary Table S1). The recombinant DyP is similar (0.48 Å RMSD, 1776 atoms) to the enzyme isolated from a fungal culture (PDB 4AU9). Moreover, most of the variants show crystal structures largely superimposable with that of WT DyP, except for the mutated residues.

The DyP structure is formed by two domains, each of them including an antiparallel four-stranded large β-sheet and two or three helices resulting in a ferredoxin-like fold (plus two additional β-strands) (Figure 1A). The C-terminal region also includes two small additional helices extending into the N-terminal domain. In spite of the obvious similarity between the two domains, only the C-terminal domain harbours a haem cofactor. His-304 (N_ε) acts as the fifth ligand of the haem iron, with Asp-395 at 2.66 Å. At the opposite side of the haem, Asp-168 and Arg-332 occupy neighbouring positions, suggesting a contribution to the haem reaction with H_2O_2. A single cysteine residue (Cys-299) is present in the C-terminal domain of DyP. The above structural characteristics of the *A. auricula-judae* and other DyPs indicate a common origin with the other members of the CDE superfamily [38] comprising chlorite dismutase [39], DyP and *E. coli* EfeB proteins [13]. Therefore similarities in the haem pocket architecture with the superfamily of classical plant/fungal/prokaryotic peroxidases [40] result from adaptive convergence to provide similar reactivity properties to the haem cofactor (see the Supplementary Results and Discussion).

Near the confluence of the two domains, a channel provides access to the haem cofactor that, due to its location in DyPs, connects to the top of the haem (Supplementary Figure S2). H_2O_2 will enter through this channel to activate the enzyme, forming compound I. However, direct oxidation of typical DyP substrates, such as RB19 and other bulky dyes, by the activated haem is not possible due to the narrow opening of the channel. Therefore LRET appears as a feasible alternative. This is in agreement with the high number of aromatic residues in the *A. auricula-judae* DyP sequence, including seven tyrosine residues and four tryptophan residues. The exposed nature of six of them (Figures 1B and 1C) suggests participation in LRET oxidation by forming reactive radicals at the protein surface. This is reminiscent of that found in ligninolytic peroxidases (LiPs and VPs) where the bulky lignin polymer is oxidized by LRET from an exposed protein radical

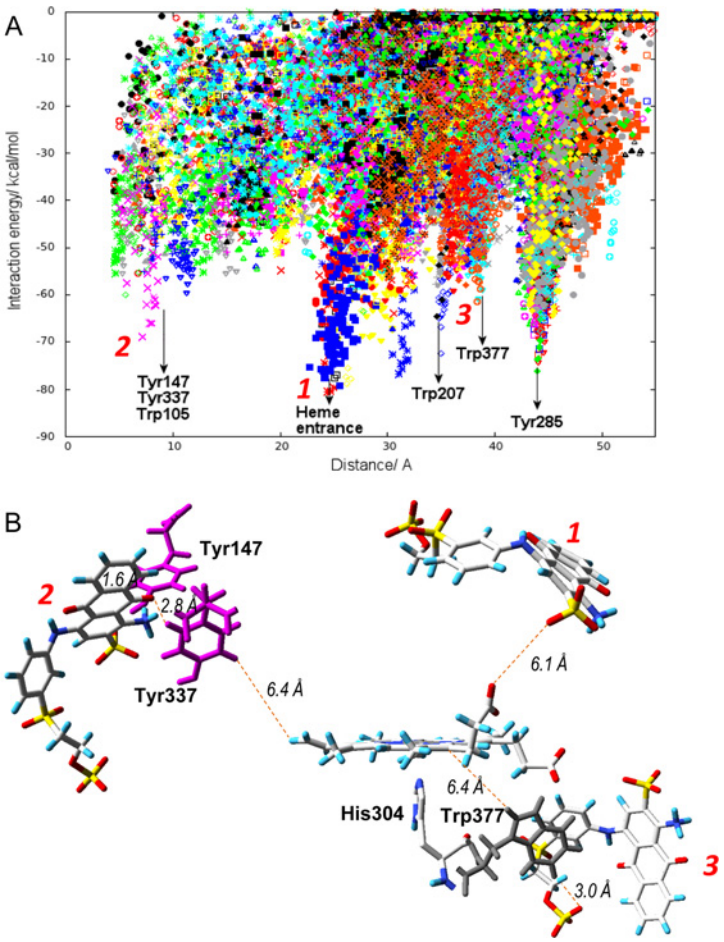

Figure 2 Substrate exploration on the DyP surface

(**A**) Local minima identified in the PELE [29] simulations of RB19 diffusion on the recombinant DyP crystal structure (PDB code 4W7J) showing interaction energy against distance to Tyr-147 (taken as a reference residue). The presence of RB19 in the vicinity of different surface residues and the haem-access channel is indicated. (**B**) Distances between the closest positions of RB19 (magenta sticks) with respect to haem (1), Tyr-147/Tyr-337 (2), and Trp-377 (3) shown by PELE (**A**), and between the above residues and the haem cofactor (the distances are measured including hydrogen atoms). RB19 is shown as CPK (Corey–Pauling–Koltun) sticks, Tyr-147/Tyr-337 as magenta sticks and Trp-377 as grey sticks.

[41–45]. Interestingly, ligninolytic peroxidases have none or only a few tyrosine residues in their sequences, a fact that has been considered as a protection against oxidative inactivation [46]. One remarkable exception is the *Trametopsis cervina* LiP that has a tyrosine residue involved in catalysis [41]. In the molecular models of other LiPs and VPs isolated from fungi or identified from genomes [20], an exposed tryptophan acts as the oxidation site for high-redox-potential aromatics, dyes and polymeric lignin via LRET [47].

Computational simulations: substrate binding (PELE) and LRET pathways (QM/MM)

To identify the possible substrate binding site(s) in *A. auricula-judae* DyP, we performed 160 PELE [29] non-biased simulations, where the typical DyP substrate RB19 was free to explore the structure of the recombinant enzyme. These simulations (Figure 2A) show that RB19 encounters several favourable docking positions on the protein surface, with local minima close to Trp-105, Tyr-147/Tyr-337, Trp-207, Tyr-285 and Trp-377 sites, as well as in the haem channel entrance. Among them, Tyr-147, Tyr337 and Trp-377 are solvent-exposed, but Trp-105 and Tyr-285 are buried into the protein (Supplementary Figure S3) making their interaction with the dye substrate more difficult. It is important to keep in mind that, whereas simulations were performed with only one substrate molecule (see Supplementary Movie S1 for an example of the exploration), under *in vitro* reaction conditions (with a large excess of substrate) multiple local minima might be populated to different extents. To address computationally which minimum will oxidize the substrate, we used QM/MM studies.

First, we performed a simple QM/MM pairwise comparison between Trp-377 and the other residues identified in the protein exploration with PELE, by including only the two selected residues in the quantum region, subtracting one electron and computing the spin density. There is a clear preference for Trp-377 to be oxidized over Trp-105, Tyr-285 and Tyr-337 (Supplementary Table S2). A comparison of Trp-207 and Trp-377 suggests that both residues could be oxidized. However, electron coupling exponentially decays with donor–acceptor distance and we can therefore exclude Trp-207 due to its large distance from the haem iron (Supplementary Figure S3). To investigate further the oxidation of Trp-377 and Tyr-337 by compound I, we performed new calculations where, in addition to these two residues, the haem was modelled as compound I and included

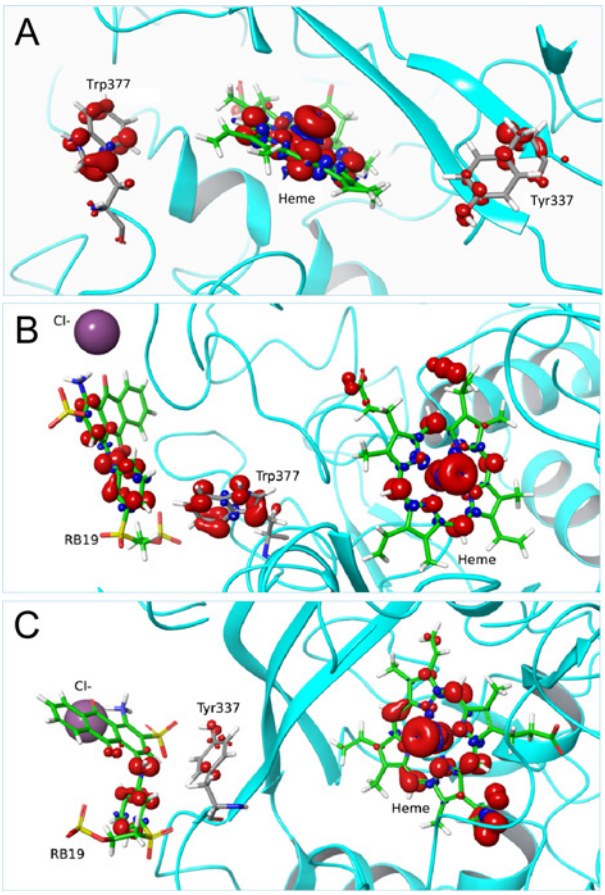

Figure 3 QM/MM electron spin distribution on Trp-377 and Tyr-337 and RB19 substrate

(**A**) Total spin density when including Trp-377, Tyr-337 and haem compound I in the quantum region (in the absence of RB19). (**B** and **C**) Total spin density when, in addition to RB19 and compound I, the quantum region includes Trp-377 or Tyr-337 respectively. From PDB code 4W7J after 5 ns MD (**A**) and selected snapshots from two energy minima showing RB19 near Trp-377 and Tyr-337, during PELE [29] diffusion in Figure 2 (**B** and **C** respectively).

in the quantum region (Figure 3A). The total spin density at Trp-377 shows its preferential oxidation by compound I, validating the previous pairwise analysis, although some density was also observed at Tyr-337.

As a final step, substrate oxidation was investigated in new calculations where we added to the quantum region RB19 at the best PELE position for each of the two residues. Figure 3(B) shows the total spin density for a structure including the dye, the surface Trp-377 and the haem cofactor. Spin density depends on the local electrostatic environment (it was previously found that Trp-377 oxidation was 40 % improved in the presence of a neighbouring Cl^- ion). In agreement with these results, the presence of anionic RB19 enhances Trp-377 oxidation. Similarly, we investigated the possibility of RB19 oxidation in the Tyr-337 site (Figure 3C), where spin density in the tyrosine and substrate are observed. Nevertheless, the most favourable residue for substrate oxidation on the protein surface is Trp-377 and so even though other surface residues may act as potential oxidizing sites, these would have a minor participation in catalysis.

Finally, using QM/MM methods, we were able to map the important residues along the LRET pathway from WT DyP Trp-377 to the haem (Figure 4). This pathway would include a first 3.0 Å electron transfer between the Trp-377 side chain and the

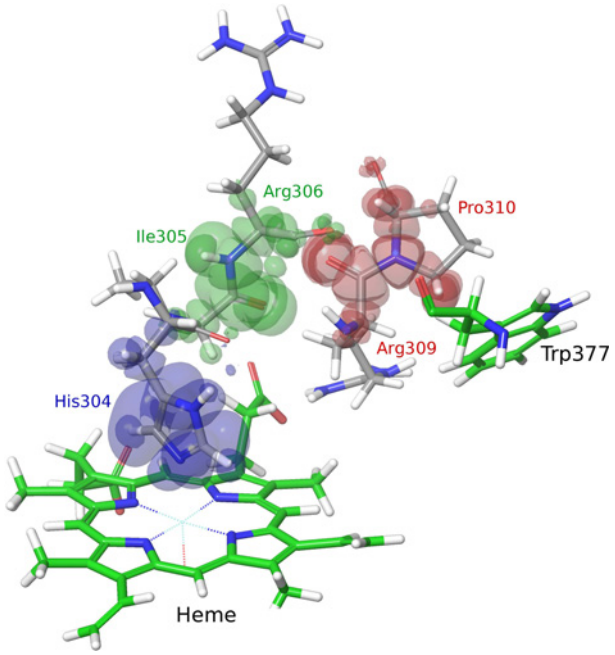

Figure 4 Electron transfer pathway from DyP Trp-377 to haem

The electron transfer pathway was obtained after three iterations of the QM/MM e-pathway approach [32] with a total of 15 residues (His-304–Arg-311, Leu-323–Ala-325, Leu-373–Gln-375 and Asp-395) included in the quantum region. Each iteration identifies the residue(s) with the highest affinity for the electron, and is shown in a different colour. The mapped route includes Pro-310 and Arg-309, followed by Arg-306, Ile-305 and His-304, as shown by the electron spin distribution.

Pro-310/Arg-309 backbone, and a second one (2.9 Å) between the Arg-309 and Arg-306 carbonyls, followed by the Arg-306 to His-304 backbone to reach the haem iron (at only 2.2 Å from the His-304 side chain). The path depicted by the QM/MM e-pathway approach [32] used in the present study is more precise than that previously predicted for the same residue using simpler geometric methods [23].

Catalytic protein radicals: EPR detection in WT DyP and mutated variants

The EPR spectrum of the WT DyP resting state (Figure 5A, top) shows a ferric species prevalently in its axial high spin state ($g_\perp \approx 6$ and $g_\parallel = 2.0$). After adding 10 eq. of H_2O_2, a strong decrease in the ferric signal, and appearance of an intense protein radical signal are evident (Figure 5A, bottom) (the electronic absorption spectra of WT DyP, and the EPR and electronic absorption spectra of the D168N and R332L variants are described in the Supplementary Results and Supplementary Figures S4 and S5 respectively). The yield of the radical observed in the spectrum of the H_2O_2-activated WT DyP is estimated as 0.58 spin/haem. Expansion of the EPR spectrum (Figure 5B) shows a protein radical signal centred at $g = 2.0041(1)$ with two low and high field components, and several sub-splittings. The overall lineshape suggests the presence of two different radical contributions, with the low field side of the spectrum less structured than the high field side, and an intense central line. To identify the radical contributions based on their different anisotropy [48–50], high-frequency EPR spectra were recorded. The narrow scan of the 94 GHz EPR spectrum of H_2O_2-activated WT DyP shows the contributions from two radicals with different g-tensor anisotropy (Figure 5C). For a tryptophanyl radical, 94 GHz EPR (3.3 T) still does not represent the high-field

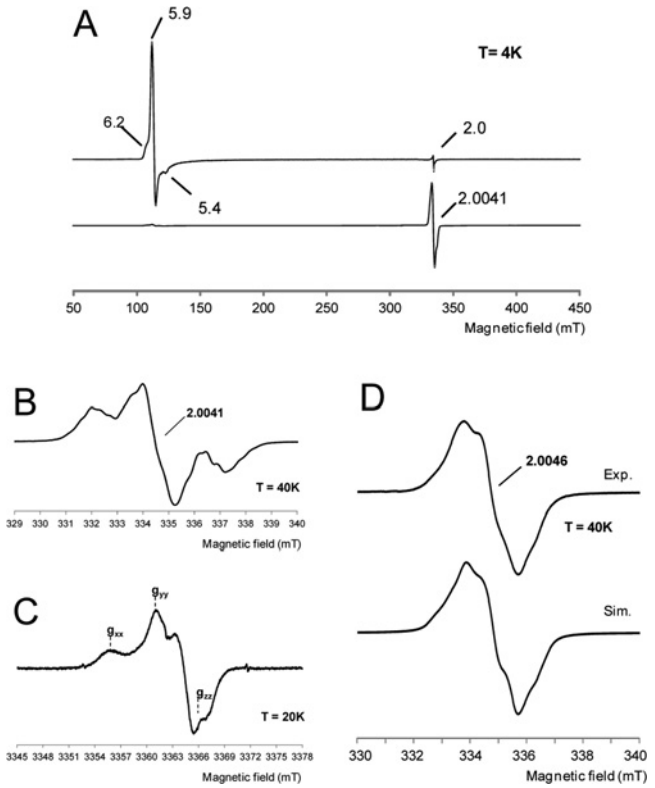

Figure 5 EPR spectra of WT DyP and its W377S variant

(**A**) X-band EPR spectra of WT DyP at pH 3 before (top) and after (bottom) the addition of H_2O_2 (and rapid freezing). Experimental conditions: $\nu = 9.39$ GHz, 0.2 mW microwave power, 0.4 mT modulation amplitude. (**B** and **C**) Narrow scan X-band ($\nu = 9.39$ GHz) and W-band ($\nu = 94.29$ GHz) respectively of the radical species. The positions of the three g-tensor components of the tyrosyl contribution are indicated. X-band experimental conditions: $\nu = 9.38$ GHz, 1 mW microwave power and 0.05 mT modulation amplitude; W-band experimental conditions: $\nu = 94.29$ GHz, 0.05 mW microwave power and 0.1 mT modulation amplitude. (**D**) X-band EPR spectrum of the radical intermediate formed in the W377S variant paired with its better simulation (Sim) (see magnetic parameters in Supplementary Table S3). Experimental conditions: $\nu = 9.39$ GHz, 1 mW microwave power, 0.2 mT modulation amplitude.

limit where the three g-tensor components are separated, whereas for tyrosyl radicals g-tensor components are well separated at 94 GHz (Figure 5C) and enabled site assignment of the protein radical.

The proof for Trp-377 being involved in the mixed protein radical was provided by the W377S variant. In the high-resolution narrow scan of its 9 GHz EPR spectrum (Figure 5D, top), the tryptophanyl contribution observed for WT DyP (Figure 5B) completely disappeared (the spectrum of the W377S/Y147S variant, not shown, being nearly superimposable). The W377S spectrum (Figure 5D, top) shows a single line with hyperfine resolution at $g = 2.0046(2)$. Simulation of this spectrum at X-band (Figure 5D, bottom) confirmed that it corresponds to a tyrosine phenoxyl radical. This identification was obtained by taking into account the experimental g-tensor component, $g_{xx} = 2.0075$ from the high-field EPR spectrum, and the hf-tensor data from the simulated 9 GHz EPR spectrum. The β-protons' hfccs agree with the computed constants for Tyr-337 (Supplementary Table S3). Therefore this residue would be responsible for the tyrosyl contribution observed in WT DyP, mixed with the main Trp-377 radical contribution.

It had been claimed that Tyr-337 was responsible for substrate oxidation by *A. auricula-judae* DyP based on spin trapping and TNM modification (see below) results [9]. Although their redox potential is affected by pH and residue environment [51], tyrosyl radicals are less reactive than tryptophanyl radicals, as shown for *P. eryngii* VP whose W164Y variant lost activity on RB5 and VA [42]. In the present study, we confirm that Tyr-337 forms a radical during H_2O_2 activation of *A. auricula-judae* DyP, but this radical represents a relatively minor contribution of the mixed tryptophanyl/tyrosyl radical signal detected (and Tyr-337 is not catalytically relevant, as discussed below) in agreement with QM/MM spin calculations. Formation of a protein radical was also suggested for *Rhodococcus jostii* DyP [14]. Tryptophanyl and tyrosyl radicals have been identified in different redox enzymes [41,47,52], and it has been suggested that both could be involved in substrate oxidation by DyPs [9,10]. In the present study, we have detected directly, for the first time, a protein radical in a DyP, whose tryptophanyl and tyrosyl contributions were identified by a combined EPR multifrequency and computational approach.

Catalytic properties after chemical modification and site-directed mutagenesis

First, the effect of pH on DyP activity was analysed (Supplementary Figure S6) and the optimal values (pH 3.5 for RB19, pH 2.5 for VA, and pH 3.0 for DMP, ABTS and RB5) were used in subsequent studies. Acidic pH optima were already reported for *A. auricula-judae* DyP [19], and are also typical of lignin-degrading peroxidases (LiP and VP) [46,53]. It is interesting that a delay period was not observed in oxidation reactions with WT DyP, and its W377S variant described below, which showed identical reaction traces and MALDI–TOF molecular masses with/without treatment with VA and H_2O_2 (Supplementary Figures S7A and S7B). This permits us to rule out in DyP an activation mechanism similar to that of *T. cervina* LiP, which enabled a tyrosine residue to oxidize high-redox-potential substrates after forming a reactive adduct with VA [54].

In a first approach for residue modification, *A. auricula-judae* DyP (3 μM) was treated with NBS, which oxidizes the tryptophan ring to oxindole [55], and TNM, which nitrates the phenolic ring of tyrosine [56]. Near 90 % activity on the four substrates assayed was removed when NBS (up to 300 μM) was used (Figure 6A). This confirms that most DyP activity is associated with tryptophan residue(s), whereas less than 15 % would be due to a different site(s). Similar TNM concentrations did not affect DyP activity, but a partial decrease was observed when a 200-fold higher concentration was used (Figure 6B, white symbols). This indicates that some tyrosine residue(s) contribute (directly or indirectly) to substrate oxidation by DyP, although to a lower extent than the tryptophan residue(s). Additional experiments analysed the effect of chemically modifying tyrosine residues on the very-low-activity W377S variant described below (Figure 6B, black symbols). Although activity decrease with some substrates (such as RB19) was observed, the activity with others (such as ABTS) was only slightly reduced, indicating that, in these cases, residues other than tyrosine residues (or maybe the haem cofactor) are involved.

An interesting initial observation, when analysing the kinetics of DyP oxidations, was the bimodal curves obtained for most substrates (Figure 7A, regions *a* and *b*). Similar sigmoidal kinetic curves were recently reported for DyP [19], and previously for *P. eryngii* VP [57]. Such curves enable calculation of two set of constants (Table 1) and reveal the existence of, at least, two oxidation sites for the same substrate. The *a* and *b* sites in *A. auricula-judae* DyP are characterized by a high turnover (k_{cat}) with low apparent affinity (as shown by the K_m values), and a low turnover with high apparent affinity respectively. The kinetic

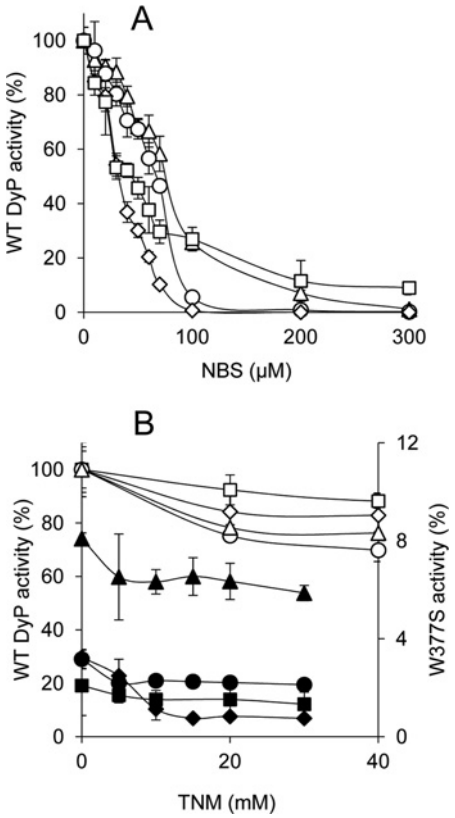

Figure 6 Chemical modification of tryptophan and tyrosine residues in WT DyP and its W377S variant

(**A**) Residual activities of 3 μM WT DyP treated with increasing NBS concentrations (in 50 mM acetate, pH 4) for modification of tryptophan residues. (**B**) Residual activities of 3 μM WT DyP and W377S variant (white and black symbols respectively) treated with increasing TNM concentrations (in 50 mM Tris/HCl, pH 7, with 2.6 % ethanol) for modification of tyrosine residues. The residual activities of the WT DyP and the W377S variant in (**A**) and (**B**) were monitored for oxidation of 180 μM RB19 (diamonds), 7.5 mM DMP (circles), 15 μM RB5 (squares) and 1.25 mM ABTS (triangles), and referred to activities of untreated WT DyP (taken as 100 %).

constants obtained show that the *A. auricula-judae* DyP is very efficient at oxidizing RB19 and ABTS dyes. However, it has lower catalytic efficiencies on DMP and RB5, and extremely low activity on VA. Finally, no Mn^{2+} oxidation activity was observed, as reported for bacterial DyPs [14,15].

Then, the exposed aromatic residues identified in PELE and QM/MM simulations were substituted to verify their eventual involvement in catalysis (information on the effect of mutating haem pocket residues is provided in the Supplementary Results). Aromatic residues were changed to serine in the simple W377S, Y147S and Y337S variants (the latter with low refolding yield). The double variant combining the last two mutations could not be refolded, but Y147F/Y337F could be obtained. Since the haem-access channel was also identified as a possible RB19-binding site (Figure 2A), the G169L variant was also obtained, whose leucine side chain completely blocks the haem-access channel, as shown in the crystal structure of a variant including the G169L mutation, compared with the WT DyP (Supplementary Figures S2B and S2A respectively).

The two sets of constants for oxidation of RB19, DMP and ABTS, and a single set for RB5 and VA, by the above five variants are shown in Table 1. The Y285F variant was also analysed, but no significant modification of the RB19 constants was observed. As a main conclusion, Trp-377 appears responsible for the high-turnover catalytic site, since its substitution (W377S variant) completely prevented high-turnover oxidation of RB19 and DMP (and decreased over 40-fold the catalytic efficiency of high-turnover ABTS oxidation). In contrast, similar Tyr-337 and Tyr-147 variants (and the double Y147F/Y337F variant) only slightly affected substrate oxidation, and did not remove the high-turnover site.

The above results are illustrated in Figures 7(A)–7(C), where kinetic plots for RB19 oxidation by WT DyP, and several tryptophan (W377S) and tyrosine (Y147S, Y337S and Y147F/Y337F) variants are shown respectively. It is observed that the DyP low-turnover site (Figure 7A, region *b*), remaining after Trp-377 removal (Figure 7B), does not correspond to Tyr-147 or Tyr-337, since changing these residues does not significantly affect the enzyme kinetics (Figure 7C). However, the disappearance of the low-turnover site in the G169L variant (Figure 7D, inset) suggests that this site involves the haem-access channel (although a decrease of the maximal turnover was also observed). Similar results were obtained for ABTS oxidation (Table 1), but the situation could be more complicated for DMP, suggesting that a third, still unidentified, site participates in oxidation of phenols by *A. auricula-judae* DyP. Finally, none of the mutations caused noticeable changes in oxidation of VA, which was highly inefficient in all cases, although Trp-377 appears to be the main residue involved.

A global view of substrate oxidation sites in the *A. auricula-judae* and other basidiomycete DyPs

The enzyme kinetics reveal the existence of at least one high-turnover and one low-turnover oxidation site in *A. auricula-judae* DyP. Site-directed mutagenesis showed that high-turnover oxidation of RB19 and other substrates by DyP takes place at the same tryptophan residue (Trp-377), identified previously as forming a protein radical. This agrees with an 85–100 % decrease in enzyme activity after modifying tryptophan residues with 0.2 mM NBS, and contrasts with the absence of a significant effect reported previously [9]. This discrepancy is probably due to the low NBS concentration used in the latter study. Modification of tyrosine residues with comparatively high TNM concentrations (40 mM) partially decreased (10–25 %) the activity of DyP, as reported previously for the enzyme purified from a fungal culture [23]. However, this does not seem to be due to modification of Tyr-337 (or contiguous Tyr-147) since the enzyme activity was practically unaffected after site-directed mutagenesis of these two residues. A possibility suggested by favourable RB19 docking by PELE is low-turnover oxidation at the DyP haem channel. Interestingly, the *B. adusta* DyP has been crystallized with DMP occupying the entrance of a second channel near the haem propionates [7]. This channel does not exist in the *A. auricula-judae* DyP, where it is covered with a loop (residues 316–324). Therefore direct substrate oxidation by the haem cofactor in the latter DyP is only possible at the main haem access channel, in agreement with results from the G169L mutation that blocked the channel. A tyrosine residue could also be responsible for the second/third catalytic sites, in agreement with the partial activity loss after TNM modification. Nevertheless, once demonstrated that Trp-377 is the main substrate oxidation site in *A. auricula-judae* DyP, it is difficult to unambiguously identify these second/third catalytic sites due to the variety of exposed aromatic residues in this haem peroxidase.

The two aromatic residues forming the mixed tryptophanyl/tyrosyl radical in the H_2O_2-activated DyP of *A. auricula-judae* (Trp-377 and Tyr-337) are not a peculiarity of this enzyme,

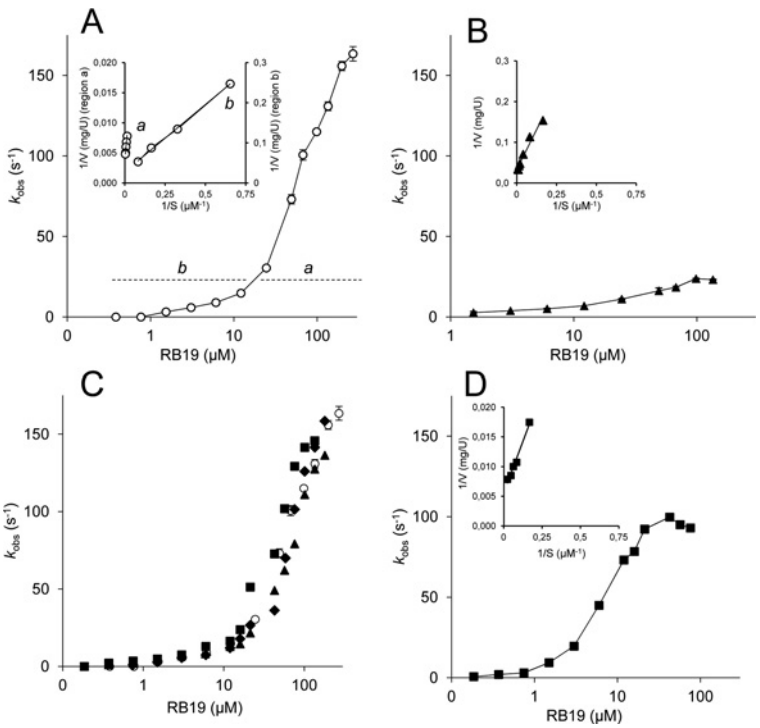

Figure 7 Kinetics for RB19 oxidation by WT DyP and different variants

(**A**) WT DyP biphasic kinetics enabling calculation of two sets of constants in the 0.2–10 μM (*b*) and 50–270 μM (*a*) ranges (inset with Lineweaver–Burk inverse representation for the high, *a*, and low, *b*, turnover sites). (**B**) Simple kinetics yielding a single set of constants (inset, inverse representation) for the W377S variant. (**C**) Results from Y147S (squares), Y337S (diamonds) and Y147F/Y337F (triangles) variants yielding kinetic curves superimposable with that of WT DyP (circles). (**D**) Simple kinetics yielding a single set of constants (inset, inverse representation) for the G169L variant. A substrate concentration logarithmic scale is used in the main plots.

Table 1 Steady-state kinetic constants of WT DyP and five site-directed variants

K_m (μM), k_{cat} (s^{-1}), and k_{cat}/K_m (s^{-1}·mM^{-1}) of WT DyP and its Trp-377, Tyr-147, Tyr-337 and Gly-169 variants oxidizing RB19, DMP, ABTS, RB5 and VA (including two sets of constants for the first four substrates corresponding to a high-turnover and a low-turnover site). Means and 95 % confidence limits from reactions at 25 °C in 0.1 M tartrate, pH 3 (pH 3.5 for RB19 and pH 2.5 for VA) using 0.1 mM H_2O_2 and 10 nM enzyme (100 nM for VA oxidation), are shown (when 1 mM H_2O_2 concentration was used, lower catalytic efficiencies were obtained, although the k_{cat} values often increased). NS, no saturation preventing kinetic constant estimation.

		WT DyP	W377S	Y147S	Y337S	Y147F/Y337F	G169L
RB19 (high turnover)	K_m	90 ± 10	–	95 ± 24	83 ± 3	130 ± 30	10 ± 3
	k_{cat}	224 ± 10	0	175 ± 24	240 ± 47	220 ± 16	106 ± 9
	k_{cat}/K_m	2460 ± 180	–	1860 ± 300	2700 ± 400	1680 ± 170	12400 ± 3000
RB19 (low turnover)	K_m	14.0 ± 2.0	3.9 ± 0.6	6.4 ± 0.8	7.4 ± 2.3	5.8 ± 0.8	–
	k_{cat}	32.0 ± 3.0	8.9 ± 0.6	26.0 ± 6.1	26.0 ± 1.9	18.0 ± 1.9	0
	k_{cat}/K_m	2230 ± 200	2240 ± 240	4070 ± 640	3370 ± 350	3200 ± 200	–
DMP (high turnover)	K_m	703 ± 61	–	763 ± 70	2840 ± 300	4720 ± 460	353 ± 41
	k_{cat}	120 ± 3	0	71 ± 2	228 ± 18	216 ± 7	88 ± 3
	k_{cat}/K_m	200 ± 18	–	93 ± 7	80 ± 1.1	46 ± 3	200 ± 21
DMP (low turnover)	K_m	6.0 ± 0.5	3560 ± 250	38.0 ± 0.4	3.1 ± 0.6	0.7 ± 0.1	6.0 ± 0.4
	k_{cat}	8.0 ± 0.2	6.4 ± 0.1	15.0 ± 0.9	8.4 ± 0.3	3.9 ± 0.1	9.9 ± 0.2
	k_{cat}/K_m	1350 ± 100	1.8 ± 0.1	397 ± 41	2730 ± 520	5900 ± 1000	1600 ± 70
ABTS (high turnover)	K_m	121 ± 7	2750 ± 470	366 ± 30	239 ± 29	173 ± 21	25 ± 2
	k_{cat}	224 ± 3	171 ± 15	311 ± 13	288 ± 10	286 ± 7.2	96 ± 2
	k_{cat}/K_m	1850 ± 94	62 ± 1	850 ± 80	1200 ± 70	1650 ± 180	3770 ± 270
ABTS (low turnover)	K_m	3.1 ± 1.1	30.0 ± 0.5	20.0 ± 6.0	2.0 ± 0.2	17.0 ± 3.6	–
	k_{cat}	7.4 ± 1.4	14.0 ± 1.0	21.0 ± 4.0	2.3 ± 0.3	21.0 ± 6.0	0
	k_{cat}/K_m	2370 ± 420	472 ± 61	1010 ± 100	1100 ± 100	1260 ± 120	–
RB5	K_m	15.6 ± 2.0	10.6 ± 1.0	15.9 ± 1.7	13.4 ± 1.7	39.0 ± 6.9	5.8 ± 0.6
	k_{cat}	4.8 ± 0.2	0.70 ± 0.02	8.3 ± 0.6	5.2 ± 0.3	9.1 ± 2.6	1.2 ± 0.1
	k_{cat}/K_m	310 ± 20	68 ± 4	525 ± 230	400 ± 29	233 ± 20	217 ± 13
VA	K_m	NS	7360 ± 1270	NS	NS	NS	NS
	k_{cat}	–	0.23 ± 0.01	–	–	–	–
	k_{cat}/K_m	0.096 ± 0.002	0.032 ± 0.003	0.101 ± 0.005	0.079 ± 0.011	0.095 ± 0.002	0.130 ± 0.006

but they are significantly conserved among basidiomycete DyPs (Supplementary Figure S8). Among the 65 DyP sequences compared, 58 include a tryptophan residue homologous with Trp-377, and 48 include a tyrosine residue homologous with Tyr-337 (whereas the neighbour Tyr-147 is only conserved in 14 sequences). Therefore the presence of exposed aromatic residues able to form catalytic radicals appears as a common characteristic of basidiomycete, and probably other, DyPs. Although involvement of tyrosyl radicals in oxidation of bulky dyes by DyP has been compared recently with oxidation of recalcitrant aromatics by tryptophanyl radicals in ligninolytic classical peroxidases [4], the results of the present study suggest that tryptophanyl radicals are mainly responsible for substrate oxidation by these two phylogenetically unrelated peroxidase types.

AUTHOR CONTRIBUTION

Dolores Linde and Cristina Coscolín performed most of the experimental biochemical work. Rebecca Pogni, Verónica Sáez-Jiménez, Maria Camilla Baratto and Adalgisa Sinicropi contributed EPR experiments and parameter calculations, simulations and interpretations. Marina Cañellas, Fátima Lucas and Victor Guallar contributed molecular docking, QM/MM and other computations. Francisco Javier Medrano and Antonio Romero contributed crystallographic structures. All authors participated in the interpretation and discussion of results. Angel Martínez, Francisco Ruiz-Dueñas, Victor Guallar and Rebecca Pogni contributed data integration and writing.

ACKNOWLEDGEMENTS

We thank the staff of the SOLEIL (Gyf-sur-Yvette, France) and ALBA (Barcelona, Spain) synchrotrons, and the BSC (Barcelona, Spain) computational facilities. The MALDI–TOF analyses were carried out at the CIB Proteomics facility, a member of the Spanish ProteoRed-ISCIII network.

FUNDING

This work was supported by the INDOX [grant number KBBE-2013-7-613549] and PELE [grant number ERC-2009-Adg 25027] European Union projects, by projects of the Spanish Ministry of Economy and Competitiveness (MINECO) [grant number BIO2011-26694, CTQ2013-48287 and BFU2011-24615] and by the Italian Ministry of Education, Universities and Research (MIUR) [project PRIN 2009-STNWX3]. D.L. and F.J.R.-D. are grateful for the financial support of an EU project contract, and a Ramón y Cajal contract of the Spanish Ministry of Economy and Competitiveness (MINECO) respectively.

REFERENCES

1 Sugano, Y. (2009) DyP-type peroxidases comprise a novel heme peroxidase family. Cell. Mol. Life Sci. **66**, 1387–1403 CrossRef PubMed
2 Hofrichter, M., Ullrich, R., Pecyna, M.J., Liers, C. and Lundell, T. (2010) New and classic families of secreted fungal heme peroxidases. Appl. Microbiol. Biotechnol. **87**, 871–897 CrossRef PubMed
3 Ruiz-Dueñas, F.J. and Martínez, A.T. (2010) Structural and functional features of peroxidases with a potential as industrial biocatalysts. In Biocatalysts Based on Heme Peroxidases (Torres, E. and Ayala, M., eds), pp. 37–59, Springer-Verlag, Berlin CrossRef
4 Colpa, D.I., Fraaije, M.W. and van Bloois, E. (2014) DyP-type peroxidases: a promising and versatile class of enzymes. J. Ind. Microbiol. Biotechnol. **41**, 1–7 CrossRef PubMed
5 Kim, S.J. and Shoda, M. (1999) Purification and characterization of a novel peroxidase from *Geotrichum candidum* Dec 1 involved in decolorization of dyes. Appl. Environ. Microbiol. **65**, 1029–1035 PubMed
6 Sugano, Y., Muramatsu, R., Ichiyanagi, A., Sato, T. and Shoda, M. (2007) DyP, a unique dye-decolorizing peroxidase, represents a novel heme peroxidase family: Asp^{171} replaces the distal histidine of classical peroxidases. J. Biol. Chem. **282**, 36652–36658 CrossRef PubMed
7 Yoshida, T., Tsuge, H., Hisabori, T. and Sugano, Y. (2012) Crystal structures of dye-decolorizing peroxidase with ascorbic acid and 2,6-dimethoxyphenol. FEBS Lett. **586**, 4351–4356 CrossRef PubMed
8 Liers, C., Pecyna, M.J., Kellner, H., Worrich, A., Zorn, H., Steffen, K.T., Hofrichter, M. and Ullrich, R. (2013) Substrate oxidation by dye-decolorizing peroxidases (DyPs) from wood- and litter-degrading agaricomycetes compared to other fungal and plant heme-peroxidases. Appl. Microbiol. Biotechnol. **87**, 5839–5849 CrossRef
9 Strittmatter, E., Liers, C., Ullrich, R., Wachter, S., Hofrichter, M., Plattner, D.A. and Piontek, K. (2013) First crystal structure of a fungal high-redox potential dye-decolorizing peroxidase: substrate interaction sites and long-range electron transfer. J. Biol. Chem. **288**, 4095–4102 CrossRef PubMed
10 Liers, C., Aranda, E., Strittmatter, E., Piontek, K., Plattner, D.A., Zorn, H., Ullrich, R. and Hofrichter, M. (2014) Phenol oxidation by DyP-type peroxidases in comparison to fungal and plant peroxidases. J. Mol. Catal. B Enzym. **103**, 41–46 CrossRef
11 Zubieta, C., Joseph, R., Krishna, S.S., McMullan, D., Kapoor, M., Axelrod, H.L., Miller, M.D., Abdubek, P., Acosta, C., Astakhova, T. et al. (2007) Identification and structural characterization of heme binding in a novel dye-decolorizing peroxidase, TyrA. Proteins **69**, 234–243 CrossRef PubMed
12 Zubieta, C., Krishna, S.S., Kapoor, M., Kozbial, P., McMullan, D., Axelrod, H.L., Miller, M.D., Abdubek, P., Ambing, E., Astakhova, T. et al. (2007) Crystal structures of two novel dye-decolorizing peroxidases reveal a β-barrel fold with a conserved heme-binding motif. Proteins **69**, 223–233 CrossRef PubMed
13 Liu, X.H., Du, Q., Wang, Z., Zhu, D.Y., Huang, Y., Li, N., Wei, T.D., Xu, S.J. and Gu, L.C. (2011) Crystal structure and biochemical features of EfeB/YcdB from *Escherichia coli* O157: Asp^{235} plays divergent roles in different enzyme-catalyzed processes. J. Biol. Chem. **286**, 14922–14931 CrossRef PubMed
14 Roberts, J.N., Singh, R., Grigg, J.C., Murphy, M. E. P., Bugg, T. D. H. and Eltis, L.D. (2011) Characterization of dye-decolorizing peroxidases from *Rhodococcus jostii* RHA1. Biochemistry **50**, 5108–5119 CrossRef PubMed
15 Brown, M.E., Barros, T. and Chang, M. C. Y. (2012) Identification and characterization of a multifunctional dye peroxidase from a lignin-reactive bacterium. ACS Chem. Biol. **7**, 2074–2081 CrossRef PubMed
16 Sugano, Y., Nakano, R., Sasaki, K. and Shoda, M. (2000) Efficient heterologous expression in *Aspergillus oryzae* of a unique dye decolorizing peroxidase, DyP, of *Geotrichum candidum* Dec 1. Appl. Environ. Microbiol. **66**, 1754–1758 CrossRef PubMed
17 Sugano, Y., Ishii, Y. and Shoda, M. (2004) Role of H164 in a unique dye-decolorizing heme peroxidase DyP. Biochem. Biophys. Res. Commun. **322**, 126–132 CrossRef PubMed
18 Liers, C., Bobeth, C., Pecyna, M., Ullrich, R. and Hofrichter, M. (2010) DyP-like peroxidases of the jelly fungus *Auricularia auricula-judae* oxidize nonphenolic lignin model compounds and high-redox potential dyes. Appl. Microbiol. Biotechnol. **85**, 1869–1879 CrossRef PubMed
19 Linde, D., Coscolín, C., Liers, C., Hofrichter, M., Martínez, A.T. and Ruiz-Dueñas, F.J. (2014) Heterologous expression and physicochemical characterization of a fungal dye-decolorizing peroxidase from *Auricularia auricula-judae*. Protein Expr. Purif. **103**, 28–37 CrossRef PubMed
20 Floudas, D., Binder, M., Riley, R., Barry, K., Blanchette, R.A., Henrissat, B., Martínez, A.T., Otillar, R., Spatafora, J.W., Yadav, J.S. et al. (2012) The Paleozoic origin of enzymatic lignin decomposition reconstructed from 31 fungal genomes. Science **336**, 1715–1719 CrossRef PubMed
21 Ahmad, M., Roberts, J.N., Hardiman, E.M., Singh, R., Eltis, L.D. and Bugg, T. D. H. (2011) Identification of DypB from *Rhodococcus jostii* RHA1 as a lignin peroxidase. Biochemistry **50**, 5096–5107 CrossRef PubMed
22 Brown, M.E. and Chang, M.C.Y. (2014) Exploring bacterial lignin degradation. Curr. Opin. Chem. Biol. **19**, 1–7 CrossRef PubMed
23 Strittmatter, E., Wachter, S., Liers, C., Ullrich, R., Hofrichter, M., Plattner, D.A. and Piontek, K. (2013) Radical formation on a conserved tyrosine residue is crucial for DyP activity. Arch. Biochem. Biophys. **537**, 161–167 CrossRef PubMed
24 Doyle, W.A., Blodig, W., Veitch, N.C., Piontek, K. and Smith, A.T. (1998) Two substrate interaction sites in lignin peroxidase revealed by site-directed mutagenesis. Biochemistry **37**, 15097–15105 CrossRef PubMed
25 Pérez-Boada, M., Ruiz-Dueñas, F.J., Pogni, R., Basosi, R., Choinowski, T., Martínez, M.J., Piontek, K. and Martínez, A.T. (2005) Versatile peroxidase oxidation of high redox potential aromatic compounds: site-directed mutagenesis, spectroscopic and crystallographic investigations of three long-range electron transfer pathways. J. Mol. Biol. **354**, 385–402 CrossRef PubMed
26 Wallrapp, F.H., Voityuk, A.A. and Guallar, V. (2013) *In-silico* assessment of protein–protein electron transfer. A case study: cytochrome *c* peroxidase – cytochrome *c*. PLoS Comput. Biol. **9**, e1002990 CrossRef PubMed
27 van der Kamp, M.W. and Mulholland, A.J. (2013) Combined quantum mechanics/molecular mechanics (QM/MM) methods in computational enzymology. Biochemistry **52**, 2708–2728 CrossRef PubMed

28 Guallar, V. and Wallrapp, F.H. (2010) QM/MM methods: looking inside heme proteins biochemisty. Biophys. Chem. **149**, 1–11 CrossRef PubMed
29 Borrelli, K.W., Vitalis, A., Alcantara, R. and Guallar, V. (2005) PELE: Protein Energy Landscape Exploration: a novel Monte Carlo based technique. J. Chem. Theory Comput. **1**, 1304–1311 CrossRef
30 Miki, Y., Ichinose, H. and Wariishi, H. (2011) Determination of a catalytic tyrosine in *Trametes cervina* lignin peroxidase with chemical modification techniques. Biotechnol. Lett. **33**, 1423–1427 CrossRef PubMed
31 Reference deleted
32 Guallar, V. and Wallrapp, F. (2008) Mapping protein electron transfer pathways with QM/MM methods. J.R. Soc. Interface **5**, S233–S239 CrossRef PubMed
33 Stoll, S. and Schweiger, A. (2006) EasySpin, a comprehensive software package for spectral simulation and analysis in EPR. J. Magn. Reson. **178**, 42–55 CrossRef PubMed
34 Aquilante, F., De Vico, L., Ferre, N., Ghigo, G., Malmqvist, P.A., Neogrady, P., Pedersen, T.B., Pitonak, M., Reiher, M., Roos, B.O. et al. (2010) Software news and update MOLCAS 7: the next generation. J. Comput. Chem. **31**, 224–247 CrossRef PubMed
35 Reference deleted
36 Bernini, C., Pogni, R., Ruiz-Dueñas, F.J., Martínez, A.T., Basosi, R. and Sinicropi, A. (2011) EPR parameters of amino acid radicals in *P. eryngii* versatile peroxidase and its W164Y variant computed at the QM/MM level. Phys. Chem. Chem. Phys. **13**, 5078–5098 CrossRef PubMed
37 Bernini, C., Andruniow, T., Olivucci, M., Pogni, R., Basosi, R. and Sinicropi, A. (2013) Effects of the protein environment on the spectral properties of tryptophan radicals in *Pseudomonas aeruginosa* azurin. J. Am. Chem. Soc. **135**, 4822–4833 CrossRef PubMed
38 Goblirsch, B., Kurker, R.C., Streit, B.R., Wilmot, C.M. and Dubois, J.L. (2011) Chlorite dismutases, DyPs, and EfeB: 3 microbial heme enzyme families comprise the CDE structural superfamily. J. Mol. Biol. **408**, 379–398 CrossRef PubMed
39 Hofbauer, S., Schaffner, I., Furtmuller, P.G. and Obinger, C. (2014) Chlorite dismutases: a heme enzyme family for use in bioremediation and generation of molecular oxygen. Biotechnol. J. **9**, 461–473 CrossRef PubMed
40 Welinder, K.G. (1992) Superfamily of plant, fungal and bacterial peroxidases. Curr. Opin. Struct. Biol. **2**, 388–393 CrossRef
41 Miki, Y., Calviño, F.R., Pogni, R., Giansanti, S., Ruiz-Dueñas, F.J., Martínez, M.J., Basosi, R., Romero, A. and Martínez, A.T. (2011) Crystallographic, kinetic, and spectroscopic study of the first ligninolytic peroxidase presenting a catalytic tyrosine. J. Biol. Chem. **286**, 15525–15534 CrossRef PubMed
42 Ruiz-Dueñas, F.J., Pogni, R., Morales, M., Giansanti, S., Mate, M.J., Romero, A., Martínez, M.J., Basosi, R. and Martínez, A.T. (2009) Protein radicals in fungal versatile peroxidase: catalytic tryptophan radical in both Compound I and Compound II and studies on W164Y, W164H and W164S variants. J. Biol. Chem. **284**, 7986–7994 CrossRef PubMed
43 Smith, A.T., Doyle, W.A., Dorlet, P. and Ivancich, A. (2009) Spectroscopic evidence for an engineered, catalytically active Trp radical that creates the unique reactivity of lignin peroxidase. Proc. Natl. Acad. Sci. U.S.A. **106**, 16084–16089 CrossRef PubMed
44 Pogni, R., Baratto, M.C., Teutloff, C., Giansanti, S., Ruiz-Dueñas, F.J., Choinowski, T., Piontek, K., Martínez, A.T., Lendzian, F. and Basosi, R. (2006) A tryptophan neutral radical in the oxidized state of versatile peroxidase from *Pleurotus eryngii*: a combined multi-frequency EPR and DFT study. J. Biol. Chem. **281**, 9517–9526 CrossRef PubMed
45 Pogni, R., Baratto, M.C., Giansanti, S., Teutloff, C., Verdín, J., Valderrama, B., Lendzian, F., Lubitz, W., Vázquez-Duhalt, R. and Basosi, R. (2005) Tryptophan-based radical in the catalytic mechanism of versatile peroxidase from *Bjerkandera adusta*. Biochemistry **44**, 4267–4274 CrossRef PubMed
46 Martínez, A.T. (2002) Molecular biology and structure–function of lignin-degrading heme peroxidases. Enzyme Microb. Technol. **30**, 425–444 CrossRef
47 Ruiz-Dueñas, F.J., Morales, M., García, E., Miki, Y., Martínez, M.J. and Martínez, A.T. (2009) Substrate oxidation sites in versatile peroxidase and other basidiomycete peroxidases. J. Exp. Bot. **60**, 441–452 CrossRef PubMed
48 Jeschke, G. (2005) EPR techniques for studying radical enzymes. Biochim. Biophys. Acta **1707**, 91–102 CrossRef PubMed
49 Bleifuss, G., Kolberg, M., Potsch, S., Hofbauer, W., Bittl, R., Lubitz, W., Graslund, A., Lassmann, G. and Lendzian, F. (2001) Tryptophan and tyrosine radicals in ribonucleotide reductase: a comparative high-field EPR study at 94 GHz. Biochemistry **40**, 15362–15368 CrossRef PubMed
50 Svistunenko, D.A., Dunne, J., Fryer, M., Nicholls, P., Reeder, B.J., Wilson, M.T., Bigotti, M.G., Cutruzzola, F. and Cooper, C.E. (2002) Comparative study of tyrosine radicals in hemoglobin and myoglobins treated with hydrogen peroxide. Biophys. J. **83**, 2845–2855 CrossRef PubMed
51 Warren, J.J., Winkler, J.R. and Gray, H.B. (2012) Redox properties of tyrosine and related molecules. FEBS Lett. **586**, 596–602 CrossRef PubMed
52 Stubbe, J. and Der Donk, W.A. (1998) Protein radicals in enzyme catalysis. Chem. Rev. **98**, 705–762 CrossRef PubMed
53 Fernández-Fueyo, E., Ruiz-Dueñas, F.J. and Martínez, A.T. (2014) Engineering a fungal peroxidase that degrades lignin at very acidic pH. Biotechnol. Biofuels **7**, 114 CrossRef
54 Miki, Y., Pogni, R., Acebes, S., Lucas, F., Fernández-Fueyo, E., Baratto, M.C., Fernández, M.I., de los Ríos, V., Ruiz-Dueñas, F.J., Sinicropi, A. et al. (2013) Formation of a tyrosine adduct involved in lignin degradation by *Trametopsis cervina* lignin peroxidase: a novel peroxidase activation mechanism. Biochem. J. **452**, 575–584 CrossRef PubMed
55 Spande, T.F., Green, N.M. and Witkop, B. (1966) Reactivity toward *N*-bromosuccinimide of tryptophan in enzymes zymogens and inhibited enzymes. Biochemistry **5**, 1926–1933 CrossRef PubMed
56 Sokolovsky, M., Riordan, J.F. and Vallee, B.L. (1966) Tetranitromethane: a reagent for nitration of tyrosyl residues in proteins. Biochemistry **5**, 3582–3589 CrossRef PubMed
57 Morales, M., Mate, M.J., Romero, A., Martínez, M.J., Martínez, A.T. and Ruiz-Dueñas, F.J. (2012) Two oxidation sites for low redox-potential substrates: a directed mutagenesis, kinetic and crystallographic study on *Pleurotus eryngii* versatile peroxidase. J. Biol. Chem. **287**, 41053–41067 CrossRef PubMed

Received 30 September 2014/10 December 2014; accepted 11 December 2014
Published as BJ Immediate Publication 11 December 2014, doi:10.1042/BJ20141211

SUPPLEMENTARY ONLINE DATA

Catalytic surface radical in dye-decolorizing peroxidase: A computational, spectroscopic and site-directed mutagenesis study

Dolores LINDE[*1], Rebecca POGNI[†1], Marina CAÑELLAS[‡§1], Fátima LUCAS[‡], Victor GUALLAR[‡¶], Maria Camilla BARATTO[†], Adalgisa SINICROPI[†], Verónica SÁEZ-JIMÉNEZ[*], Cristina COSCOLÍN[*], Antonio ROMERO[*], Francisco Javier MEDRANO[*], Francisco J. RUIZ-DUEÑAS[*2], and Angel T. MARTÍNEZ[*2]

[*]Centro de Investigaciones Biológicas, CSIC, Ramiro de Maeztu 9, E-28040 Madrid, Spain, [†]Department of Biotechnology, Chemistry and Pharmacy, University of Siena, I-53100, Siena, Italy, [‡]Joint BSC-CRG-IRB Research Program in Computational Biology, Barcelona Supercomputing Center, Jordi Girona 29, E-08034 Barcelona, Spain [§]Anaxomics Biotech, Balmes 89, E-08008 Barcelona, Spain and [¶]ICREA, Passeig Lluís Companys 23, E-08010 Barcelona, Spain

Supplementary methods for DyP production, activation and purification; supplementary results and discussion on electronic absorption and EPR spectra of WT DyP and haem pockets variants; three supplementary tables providing the crystallographic data (**Table S1**), spin density in pairwise comparison of Trp-377 and other residues (**Table S2**) and experimental and computed g-tensors and hfcc values for Tyr-337 radical species (**Table S3**); eight supplementary figures showing the chemical structures of the five DyP substrates assayed (**Fig. S1**), the haem access channel region in WT DyP and after G169L mutation (**Fig. S2**), the location of several tryptophan and tyrosine residues with respect to the haem cofactor (**Fig. S3**), the electronic absorption spectra of WT DyP (**Fig. S4**), the electronic absorption and EPR spectra of the D168N and R332L variants (**Fig. S5**), the optimal pH for DyP oxidation of different substrates (**Fig. S6**), kinetic and MALDI-TOF evidence for lack of a DyP activation mechanism (**Fig. S7**), Tyr-147, Tyr-337 and Trp-377 homolog residues in different clusters of basidiomycete DyP phylogram (**Fig. S8**), and conserved tryptophan and tyrosine residues in several basidiomycete DyPs (**Fig. S9**); one supplementary movie showing a PELE trajectory for RB19 free diffusion on DyP (**Movie S1**); and references for supplementary data are included below.

SUPPLEMENTARY METHODS

Chemicals

DNaseI, polymerase, and NBS were from Boehringer-Mannhein, Roche and Fluka, respectively. Bactopeptone and yeast extract were from Difco. *Nde*I and *Bam*HI were from New England Biolabs. Ampicillin, chloramphenicol, dithiothreitol, hemin, isopropyl-β-D-thiogalactopyranoside, lysozyme, sodium tartrate and TNM were from Sigma-Aldrich. Other chemicals were from Merck.

DyP production, activation and purification

E. coli BL21(DE3)pLysS cells with the pET23a-DyPI vector containing the *A. auricula-judae* mature WT DyP sequence (and those of DyP variants) were grown overnight at 37 ºC and 170 rpm in Luria Bertani broth (with 100 μg/mL of ampicillin and 34 μg/mL of chloramphenicol), and used to inoculate 2 L flasks containing 1 L of Terrific Broth (with ampicillin and chloramphenicol) that were grown for 3 h at 37 ºC and 200 rpm, induced with 1 mM isopropyl-β-D-thiogalactopyranoside, grown for further 4 h, and harvested by centrifugation.

---

[1]These authors contributed equally to this work

[2]To whom correspondence may be addressed: CIB, CSIC, Ramiro de Maeztu 9, E-28040 Madrid, Spain. Tel.: +34 918373112, Fax: +34 915360432 E-mail: ATMartinez@cib.csic.es and fjruiz@cib.csic.es.

The apoenzyme accumulated in inclusion bodies was solubilised in 50 mM Tris-HCl (pH 8.0) containing 8 M urea, 1 mM EDTA, and 1 mM dithiothreitol for 1 h at 4ºC. Subsequent "in vitro" activation was performed at 4 ºC using 0.2 M urea, 10 μM hemin, 0.02 mM dithiothreitol, 0.1 mM EDTA and 0.1 mg/ml of protein in 50 mM phosphate (pH 6). After 144 h, the folding mixture was concentrated, dialyzed against 20 mM sodium acetate (pH 4.3), and the insoluble material eliminated by centrifugation (13000 rpm, 30 min).

WT DyP and its site-directed variants were purified using a Resource Q column (GE Healthcare) coupled to an ÄKTA liquid chromatography system, using a gradient from 0 to 0.3 M of NaCl in 10 mM Tris-HCl (pH 7). DyPs were analyzed by SDS-PAGE to confirm the purity of the proteins. Absorption spectra were recorded in 10 mM sodium tartrate (pH 5) at 25 ºC in a Thermo Spectronic diode-array spectrophotometer. The DyP molar absorption coefficient (ε_{405} 117000 $M^{-1}\cdot cm^{-1}$) was calculated from (triplicate) Bradford determination of protein concentration, and used to estimate enzyme concentrations. For spectroscopic characterization of the transient states in the DyP catalytic cycle 1-10 eq of H_2O_2 were added to the resting enzyme in 10 mM sodium tartrate (pH 3 and 7).

Site-directed mutagenesis: Primers and PCR conditions

For PCR mutagenesis, direct and reverse primers designed complementary to opposite strands of the DNA region containing the desired mutation were used. The sequences of the direct primers (with the mutated codons in italics) used for mutagenic PCR was the following: Y147S or Y147F mutations 5´-CG TCG ATC TCG AAG CTC (*TCT* or *TTC*, respectively) TCG TTG TCG GCT TCG-3´; D168N mutation, 5´-G TTC GGC TTC CTT *AAC* GGA ATT GCT CAG CC-3´; G169L mutation, 5´-C GGC TTC CTT GAT *CTT* ATT GCT CAG CCC GC-3´; Y285F mutation, 5´-GG AAC AAC AAC TTC ACC *TTC* TCA CAC GCC G- 3´; Y337S or Y337F mutations, 5´-GGC ATC CCC (*TCT* or *TTC*, respectively) GGT CCT GAG GTT ACC-3´; and W377S mutation, 5´-C CTT CAG CAG ACG *TCT* GCC GAT AAC GCC AAC TTC CC-3´.

PCR reactions were carried out in an Eppendorf (Hamburg, Germany) Mastercycler Pro using 10 ng of template DNA, 250 μM each dNTP, 125 ng of direct and reverse primers, 2.5 units of polymerase (Expand Long Template PCR System), and the manufacture´s reaction buffer. Reaction conditions were as follows: i) a “hot start” of 95 ºC for 1 min; ii) 18 cycles at 95 ºC for 50 s, 55 ºC for 50 s, and 68 ºC for 10 min; and iii) a final cycle at 68 ºC for 10 min. The mutated sequences were confirmed by DNA sequencing using an ABI 3730 DNA Analyzer (Applied Biosystem).

Chemical modification

TNM in ethanol (0-40 mM and 0-30 mM for WT DyP and its W377S variant, respectively) or NBS (0-300 μM) were added to 3 μM enzyme in 50 mM Tris-HCl (pH 7) or 50 mM acetate (pH 4), respectively. The final concentration of ethanol in the TNM modification mixture was 2.6%. After 30 min of incubation at 25ºC, the samples were applied into a 30 kDa Centricon Millipore and diafiltrated with 3 vol of 10 mM tartrate (pH 5).

DyP crystallization, data collection and refinement

Crystallization trials with WT DyP and its site-directed variants (Y147S, D168N, W377S,Y147S/W377S and Y147S/G169L/W377S) were carried out by the sitting drop vapor diffusion method, in 96-well MRC2 plates with 50 μl reservoir solution, using the Emerald (Wizard screens I-III) and Jena Biosciences screenings (JBScreen kits 1-10) at 22 ºC. Drops consisted of 0.2 μl of protein solution (10 mg/ml in 10 mM sodium tartrate, pH 5.0) and 0.2 μl of reservoir solution. Crystals of WT DyP were obtained in 32.5% PEG 4000, and crystals of all the site-directed variants were obtained in PEG 2000 MME (30 to 35%).

The crystals were mounted in nylon loops and flash-frozen in liquid N_2 in the mother liquor using Paratone-N (Hampton Research) as cryoprotectant. X-ray diffraction intensities were collected (100 K) at the PROXIMA-1 beam line at SOLEIL (Gyf-sur-Yvette, France), and at XALOC beam line at

ALBA (Barcelona, Spain) using a Pilatus 6M detector. Data were indexed, integrated, merged and scaled using XDS and XSCALE [1].

The structure of DyP was solved by molecular replacement using the crystal structure of *B. adusta* DyP (PDB entry 4AFV) as the search model and the program AUTOMR of the PHENIX package [2]. The final model was obtained by successive refinement rounds (PHENIX package) followed by manual building with Coot [3] using σ_A weighted 2Fo-Fc and Fo-Fc electron density maps. Solvent molecules were introduced in the refinement, as implemented in the PHENIX package, and visually inspected. A total of 5% of reflections was used to calculate the R_{free} value throughout the refinement process. The structures of all the variants were solved using that of WT DyP as a model, and the final models were obtained in the same way as explained above. The structures were validated with MolProbity [4]. PyMOL [5] and Deep view/Swiss Pdb-Viewer (www.expasy.org/spdbv) were used for structure visualization and analysis, and image generation.

Enzyme kinetics

Steady-state kinetic constants of WT DyP and its site-directed variants on five selected substrates (whose structures are shown in **Fig. S1**) were determined using a Thermo Spectronic UV-visible spectrophotometer. For DMP, ABTS and VA oxidation, absorbance increases at 469 nm (dimeric coerulignone ε_{469}= 55,000 cm^{-1} M^{-1}), 436 nm (ABTS cation radical ε_{436}= 29,300 cm^{-1} M^{-1}) and 310 nm (veratraldehyde ε_{310}= 9,300 cm^{-1} M^{-1}) were followed, respectively. Absorbance decreases were followed in the cases of RB5 (ε_{598}= 30,000 cm^{-1} M^{-1}) and RB19 (ε_{595}= 10,000 cm^{-1} M^{-1}) oxidation resulting in dye decolorization. The ability to oxidize Mn^{2+} was investigated by the eventual formation of Mn^{3+}·tartrate complex (ε_{238} 6500 cm^{-1} M^{-1}) in 0.1 M tartrate (pH 5). Reactions were performed at 25 ºC in 100 mM tartrate, pH 3, except for VA and RB19 oxidation that pH 2.5 and 3.5 were used, respectively. All the substrates were tested using the enzymes at a final concentration of 10 nM (except VA whose oxidation was assayed with 100 nM enzyme) and 0.1 mM H_2O_2. Apparent affinity constant (Michaelis–Menten constant, K_m), turnover number (catalytic constant, k_{cat}) and their standard errors were obtained by non-linear least-squares fitting of the experimental measurements to the Michaelis-Menten model. The catalytic efficiency (k_{cat}/K_m) values with their standard errors were calculated fitting the experimental data to the normalized Michaelis-Menten equation: $v= (k_{cat}/K_m)[S]/(1+[S]/K_m)$. The catalytic efficiency constant for VA was obtained by fitting data to a linear regression equation ($k_{cat}= (k_{cat}/K_m)[S]$) since no enzyme saturation was attained.

MALDI-TOF after steady-state turnover

Eventual changes in the molecular mass of WT DyP, similar to those produced during activation of the *T. cervina* LiP by formation of a VA adduct with the catalytic tyrosine residue, were analyzed by MALDI-TOF using an Autoflex III instruments, and 2,5-dihydroxyacetophenone matrix, after enzyme reaction with H_2O_2 and VA, as previously described [6]. For these analyses, 10 μM enzyme was incubated for 1 h at 25 °C, in sodium tartrate (pH 3) containing 0.5 mM H_2O_2 and 10 mM VA, and compared with a control without H_2O_2 and VA. The reaction mixture was centrifuged into a 30 kDa Centricon Millipore, diafiltrated with 3 vol of 20 mM tartrate (pH 5).

Computational analyses: PELE, MD and QM/MM calculations

The model used is based on the recombinant *A. auricula-judae* DyP crystal structure solved here. As the optimum pH for oxidation of RB19 by DyP is 3.5 we prepared the starting structure accordingly. All ionizable residues were inspected with Schrodinger's protein preparation wizard [7] and with the H++ web server [8]. His-304 was assessed to be δ-protonated, His-115 ε-protonated, and the remaining are double protonated (positively charged). At this low pH several aspartic (residues 8, 12, 84, 129, 189, 246 and 270) and glutamic (residues 158, 220, 225 and 432) acids are in their acidic form, while all other ones are found in their anionic states. Electrostatic potential atomic charges on the RB19 substrate (**Fig. S1A**), to be used in PELE and molecular

dynamics (MD), were obtained from an optimization with Jaguar [9] at the DFT/M06-L level with the 6-31G** basis set and a PB implicit solvent.

Once the initial protein structure was prepared, RB19 was placed manually in 20 initial random positions on the protein's surface and the protein-ligand conformational space was explored with PELE [10]. This is a Monte Carlo based algorithm that produces new configurations through a sequential ligand and protein perturbation, side chain prediction and minimization steps. New configurations are then filtered with a Metropolis acceptance test, where the energy is described with an all-atom OPLS force field and a surface generalized Born solvent. In this way it is possible to locate and characterize local and global minima structures for the most favorable protein-ligand interactions. Results shown are based on 160 independent 48-h PELE simulations. Enhanced local sampling on Trp-377 surface site was obtained with a 5 ns MD simulation with DESMOND [11]. Such analysis allowed us to investigate the effect of solvent and charge fluctuations on the oxidative tendency of Trp-377 and RB19.

QM/MM calculations were performed with Qsite [12]. This method allows for the incorporation of the complete protein structure (as well as solvent and ions) at the atomic level while electronic structure based methods are employed in a sub-section of the system. Most calculations were performed at the M06-L(lacvp*)/OPLS level. Spin densities for the highly reactive compound I were computed at the quartet spin state (easier to converge than the isoenergetic doublet one). Spin density on residues was computed by adding all the atomic spin density contributions. Those residues included in the QM region with/without the haem cofactor (compound I) and a substrate (RB19) molecule are indicated in each case. Additionally, electron transfer pathway calculations were performed with the QM/MM e-pathway approach (using the Hartee-Fock method) [13]. This approach maps those residues with higher probability to participate in the electron transfer pathway by finding, iteratively, those regions of the transfer region with lower ionization energy. In particular, we computed the pathway from Trp377 by considering in the QM region His-304, Ile-305, Arg-306, Lys-307, Thr-308, Arg-309, Pro-310, Arg-311, Leu-323, Ser-324, Ala-325, Leu-373, Gln-374, Gln-375 and Asp-395.

EPR equipments

CW X-band (9.8 GHz) measurements were performed with a Bruker E500 Elexsys Series using the Bruker ER 4122SHQE cavity, equipped with an Oxford helium continuous flow cryostat (ESR900). W-band (94.17 GHz) experiments were recorded on a Bruker Elexsys E600 spectrometer, operating in continuous wave, equipped with a 6T split-coils superconducting magnet (Oxford Instrument), using a continuous helium flow cryostat (Oxford Instrument).

SUPPLEMENTARY RESULTS AND DISCUSSION

Haem pocket site-directed variants: Electronic absorption and EPR spectra

Asp-168 in DyP occupies the position of conserved distal histidine in classical peroxidases. This residue and the neighbor Arg-332 are expected to play a central role in catalysis since both the D168N and the R332L variants obtained were fully inactive on the different substrates.

The electronic absorption spectra of DyP resting and H_2O_2-activated (2 eq) states at pH 3 (the optimal pH for DyP activity, as shown in **Fig. S6**) are included in **Fig. S4A**. The latter exhibit the main peak at 403 nm, and small maxima at 529, 558, 597 and 620 nm, all of them being characteristic for compound I. However, the D168N and R332L variants were unable to react with H_2O_2 (pH 3) as shown by their unchanged absorption spectra (**Fig. S5A** and **B**). When 2 eq of H_2O_2 were added to the resting enzyme at pH 7 (which showed reduced absorbance at 406 and 630 nm and the 506 nm maximum displaced to 502 nm with respect to the pH 3 resting state) a compound II-like spectrum, with main peak at 418 nm and small maxima at 530, 554 and 634 nm, was obtained (**Fig. S4B**). Unexpectedly, no compound II-like spectrum could be obtained at pH 3 by self-reduction or using other H_2O_2 concentrations.

The involvement of Asp-168 and Arg-332 in DyP reactivity with H_2O_2, suggested by the electronic absorption spectra, was investigated by EPR. The resting state spectrum of the D168N variant showed a ferric iron in a rhombic environment (g_{xx}= 6.06, g_{yy}=5.6 and g_{zz}= 2.0) (**Fig. S5C**, black trace). After H_2O_2 activation at pH 3 (**Fig. S5C**, red trace) only a small decrease in the ferric iron signal is recorded and no protein radicals are formed. An almost undetectable amount of compound I in the form of the porphyrin radical can be identified superimposed to the ferric g= 2 region of the EPR spectrum (**Fig. S5C**, inset). The results were similar for the R332L variant (**Fig. S5C**), although a small radical signal was observed (4% radical yield for R332L at pH 3 compared with 58% for WT DyP, under the same experimental conditions) (**Fig. S5D**, inset).

The similarities in the haem pocket architecture of unrelated DyP and classical (plant-fungal-prokaryotic) peroxidases would result from adaptative convergence. This is the case of: i) the conserved proximal histidine (*A. auricula-judae* DyP His-304) acting as the fifth haem iron ligand in both enzyme types; and ii) the opposite haem side residues (DyP Asp-168 and Arg-332) most probably contributing to reaction with H_2O_2, as distal histidine and arginine do in classical peroxidases. The latter was demonstrated by the loss of DyP ability to form compound I after the D168N and R332L mutations (as shown by electronic absorption and EPR spectra). A central role of the conserved aspartic acid or arginine in H_2O_2 reaction have been claimed in the *B. adusta* [14] and *R. jostii* DyP [15], respectively, but the present results show that both residues are required for *A. auricula*-judae DyP activity, although some protein radical signal was still observed in the EPR spectrum of the R332L variant. As reported for other DyPs [14], no compound II spectrum was observed during self-reduction of the *A. auricula-judae* DyP (at physiological pH 3), a fact that suggests fastest self-reduction of compound II than of compound I, in contrast with other fungal peroxidases [16]. At the other side of the haem, Asp-395, also conserved in other DyPs [14], would help proximal His-304 to modulate the haem electron-deficiency, as the proximal aspartic acid in classical peroxidases [17].

SUPPLEMENTARY TABLES

Table S1 Data collection and refinement statistics of *A. auricula-judae* WT DyP expressed in *E. coli* and five site-directed variants

	WT DyP	Y147S	D168N	W377S	Y147S/W377S	Y147S/G169L/ W377S
Data collection						
Space group	C2	C2	C2	C2	C2	C2
Cell constants:						
-a (Å)	154.2	184.0	183.7	184.0	154.2	104.4
-b (Å)	100.5	55.9	56.3	56.2	100.5	56.1
-c (Å)	128.6	104.0	103.8	104.1	128.6	82.0
-β (º)	123.7	118.3	117.8	118.0	123.7	96.9
Resolution range (Å)	50.00-1.79 (1.89-1.79)[a]	50.00-1.05 (1.11-1.05)	50.00-1.05 (1.11-1.05)	50.00-1.15 (1.22-1.15)	50.00-1.40 (1.49-1.40)	50.00-1.20 (1.27-1.20)
Total reflections	620794	2174931	2352392	1894778	1142801	949627
Unique reflections	150630	364516	405267	319222	181153	147432
R_{merge} (%)	13.4 (99.5)	8.8 (105.2)	6.8 (50.5)	6.6 (38.4)	7.0 (97.2)	6.0 (45.8)
CC1/2	99.7 (70.5)	99.9 (45.3)	99.9 (82.3)	99.8 (87.3)	99.9 (71.1)	99.9 (93.8)
Completeness (%)	97.1 (90.3)	82.6 (29.8)	91.5 (54.3)	95.2 (72.1)	99.3 (96.8)	99.2 (95.4)
$\langle I/\sigma(I) \rangle$	6.59 (1.03)	12.3 (1.0)	12.7 (1.7)	13.1 (2.3)	14.2 (1.5)	15.4 (3.1)
Multiplicity	4.1 (3.5)	6.0 (2.9)	5.8 (3.3)	5.9 (3.5)	6.3 (5.2)	6.4 (6.1)
Subunits/asymmetric unit	4	2	2	2	2	1
Wilson B factor (Å^2)	21.52	10.27	8.91	15.35	23.44	12.07
Refinement						
Resolution range	50.00-1.79	50.00-1.05	50.00-1.05	50.00-1.15	50.00-1.79	50.00-1.20
Working reflections	150153	364071	405142	319118	150153	146680
R_{work}/R_{free}	0.193/0.240	0.135/0.157	0.131/0.150	0.131/0.150	0.144/0.184	0.139/0.158
Protein atoms (non H)	13217	6705	6721	6586	6663	3302
Haem group	172	94	94	86	86	43
Water molecules	1564	1582	1887	1156	1489	700
Mean B factors (Å^2):						
-Protein atoms (non H)	24.83	11.86	10.46	17.16	12.65	15.04
-Haem group	19.66	7.90	6.97	10.99	9.27	10.07
-Water molecules	30.29	24.91	23.35	29.60	24.58	27.80
Deviations from ideality:						
-rmsd bond lengths (Å)	0.009	0.009	0.010	0.004	0.009	0.007
-rmsd angles (º)	1.210	1.410	1.432	0.930	1.210	1.257
Ramachandran statistics:						
-Preferred (%)	97.86	98.54	98.66	98.76	98.42	98.87
-Allowed (%)	2.03	1.46	1.23	1.20	1.58	1.13
-Outliers (%)	0.11	0.00	0.11	0.00	0.00	0.00
PDB code	4W7J	4W7K	4W7L	4W7M	4W7N	4W7O

[a]Data in parenthesis correspond to the last resolution layer.

Table S2 Spin density in pairwise QM/MM comparison of Trp-377 and other surface residues

Pairwise comparisons of spin density distribution in Trp-377 and other surface residues at different distances to haem of *A. auricula-judae* DyP were performed by QM/MM calculations (the distances, in parentheses, are between the residue gamma carbon and the haem iron).

Residue 1	Spin (%)	Residue 2	Spin (%)
Trp-377 (12.5 Å)	100	Trp-105 (19.5 Å)	0
Trp-377	38	Trp-207 (32.0 Å)	62
Trp-377	100	Tyr-285 (14.5 Å)	0
Trp-377	100	Tyr-337 (15.9 Å)	0

Table S3 Comparison of experimental (from W377S variant) and computed (for DyP Tyr-337) tyrosine radical EPR parameters

Experimental (W377S variant) and B3LYP/EPR-II g-tensors (g_i) and hfcc values (A_i, in MHz) computed at the B3LYP/AMBER optimized geometries for Tyr-337 radical species are shown.

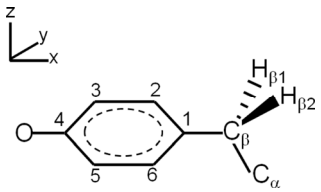

			[a]g_i	$A_i(H_{\beta1})$	$A_i(H_{\beta2})$	$A_i(H_2)$	$A_i(H_6)$	$A_i(H_3)$	$A_i(H_5)$
W377S		x	2.0075	16.6	15.4	2.0	2.7	26.0	24.0
		y	2.0043	17.3	16.0	4.5	5.2	21.0	19.0
		z	2.0020	22.4	21.0	8.1	9.0	7.0	7.0
		Iso	2.0046	18.8	17.5	4.9	5.6	18.0	16.6
B3LYP/EPR-II[b]	Tyr-337$^{\bullet}$	x	2.0066	16.6	15.4	2.0	2.7	-26.3	-24.2
		y	2.0044	17.3	16.1	4.5	5.2	-20.3	-18.7
		z	2.0022	22.4	21.5	8.1	9.0	-6.6	-5.7
		Iso	2.0044	18.8	17.7	4.9	5.6	-17.8	-16.2

[a]The errors on the experimental g values are: $\pm$ 0.0001 for g_x, $\pm$ 0.0002 for g_y and g_z; [b]The computed hfcc values for Tyr-337 radical have been used to simulate the experimental EPR spectrum of the radical species in the W377S variant. Although the B3LYP/EPRII g_x value differs from the experimental one, the computed values clearly indicate that the tyrosine radical is embedded in a strongly H-bonded environment, which is in accord with the experiments.

SUPPLEMENTARY FIGURES

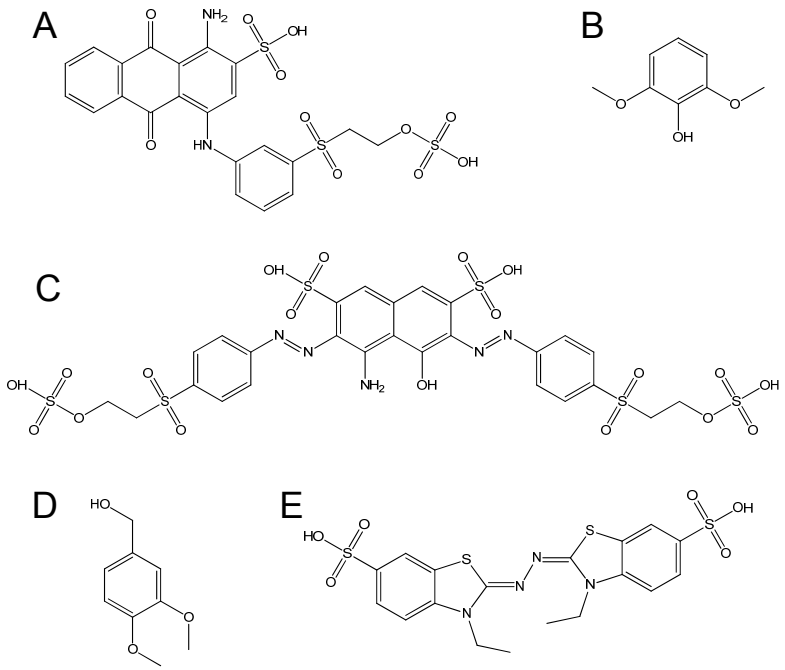

Figure S1 Chemical structure of the five DyP substrates assayed
(A) RB19 (1-amino-9,10-dioxo-4-((3-((2-(sulfooxy)ethyl)sulfonyl)phenyl)amino)-9,10-dihydroanthracene-2-sulfonic acid). **(B)** 2,6-Dimeth-oxyphenol. **(C)** RB5 (4-amino-5-hydroxy-3,6-bis((E)-(4-((2-(sulfooxy)ethyl)sulfonyl)phenyl)-diazenyl)-naphthalene-2,7-disulfonic acid). **(D)** Veratryl (3,4-dimethoxybenzyl) alcohol. **(E)** ABTS (2,2'-azino-bis(3-ethylbenzothiazoline-6-sulphonic acid).

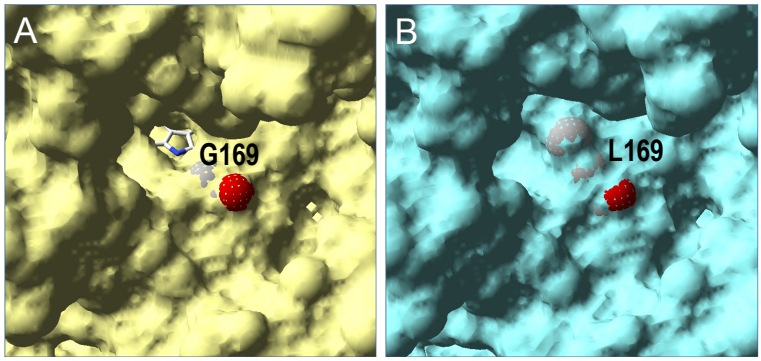

Figure S2 Haem access channel region in WT DyP and after G169L mutation
(A) Solvent access surface in the WT DyP crystal structure (PDB 4W7J) showing channel accessing to the haem cofactor (CPK sticks) and the position of Gly-169 (CPK spheres). **(B)** Solvent access surface in the C169L/Y146S/W377S variant (PDB 4W7O) showing the blocked haem access by the Leu-169 (CPK spheres) side-chain.

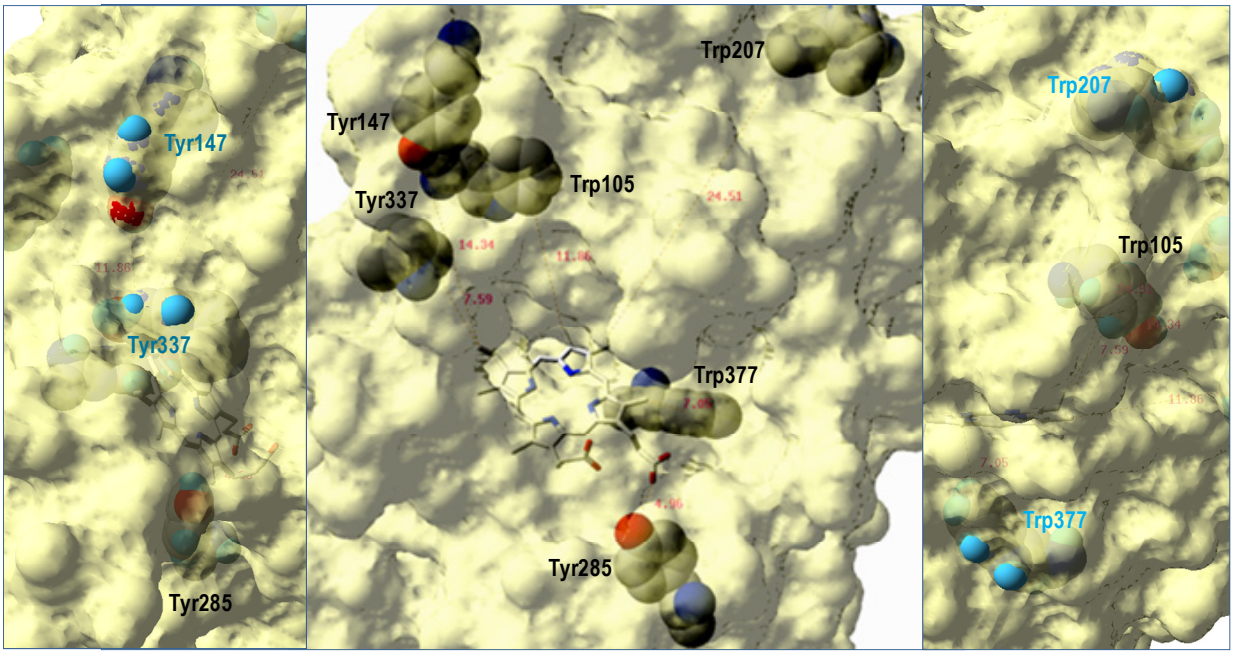

Figure S3 Location of several tryptophan and tyrosine residues near the haem cofactor of DyP.

(center) Semitransparent DyP surface showing the channel accessing the haem cofactor (CPK sticks) and the position of Trp-105, Tyr-147, Trp-207, Tyr-285, Tyr-337 and Trp-377 (CPK spheres) at 12, 14, 25, 5, 8 and 7 Å from the cofactor, respectively. ***(left*** and ***right)*** Exposed Tyr-147, Trp-207, Tyr-337 and Trp-377, and buried Trp-105 and Tyr-285 (CPK spheres with H atoms included). From PDB 4W7J.

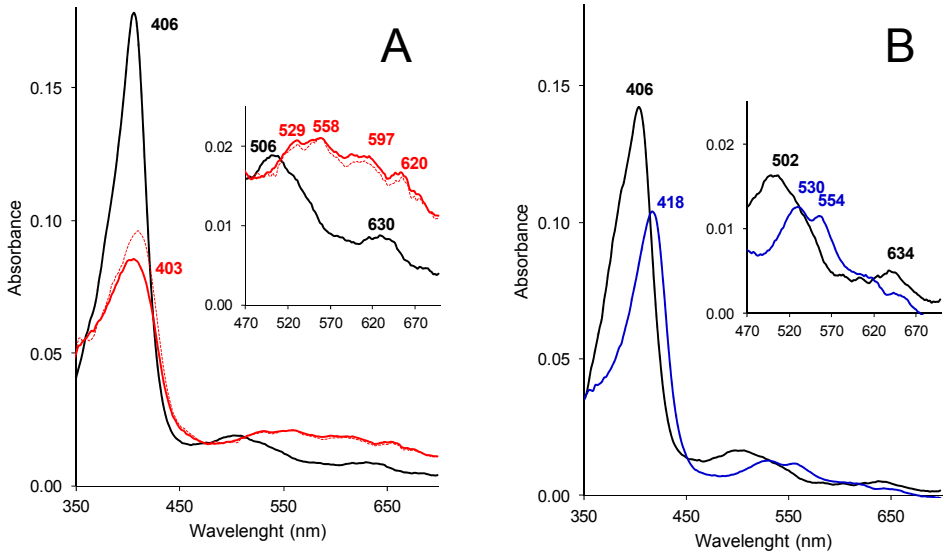

Figure S4 Electronic absorption spectra of DyP

(A) Compound I spectrum (red) obtained 2 s after addition of 2 eq of H_2O_2 to DyP resting state (black) in 10 mM tartrate, pH 3, showing the main Soret band at 403 and 406 nm, respectively, and small charge transfer bands in the inset (dotted line shows the spectrum obtained 0.02 s after H_2O_2 addition). **(B)** Compound II-like spectrum (blue) obtained 2 s after addition of 2 eq of H_2O_2 to DyP resting state (black) in 10 mM Tris-HCl, pH 7, showing the main Soret band at 418 and 406 nm, respectively, and small charge transfer bands in the inset. Spectra were obtained using a stopped-flow rapid spectrophotometer (Bio-Logic) equipped with three-syringe module (SFM300), diode array detector (J&M), and Bio-Kine software.

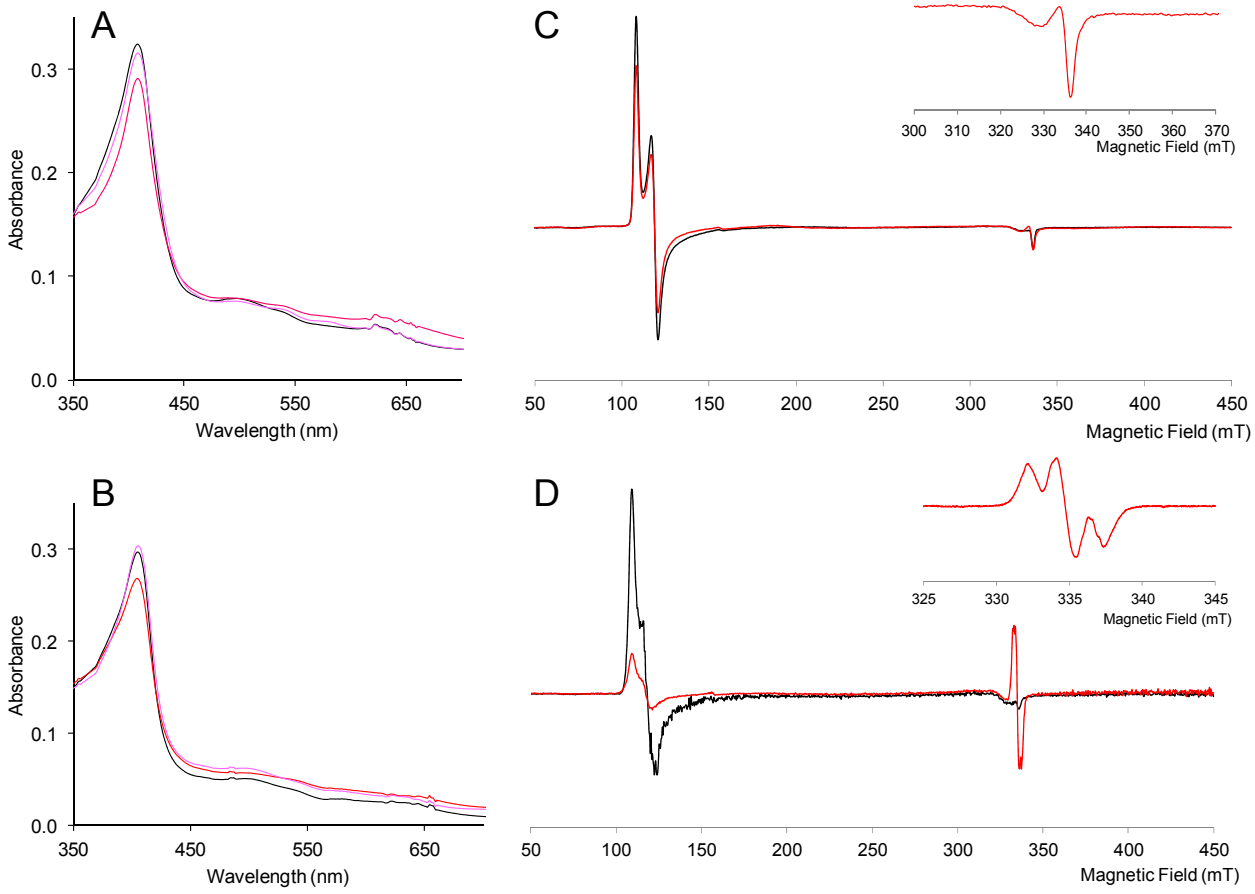

Figure S5 Electronic absorption and EPR spectra of peroxide-activated D168N and R332L variants

(A and **B)** Electronic absorption spectra of 10 µM D168N and R332L variants 0 (black), 50 (red) and 1600 (pink) s after addition of 10 eq of H_2O_2 in 10 mM tartrate, pH 3, respectively. **(C** and **D)** X-band EPR spectra of the D168N and R332L variants (160 µM) before (black) and after (red) addition of 10 eq of H_2O_2 in 70 mM tartrate, pH 3, respectively (insets, detail of the g= 2 region). Experimental conditions: v= 9.39 GHz, 2 mW microwave power, 0.4 mT modulation amplitude)

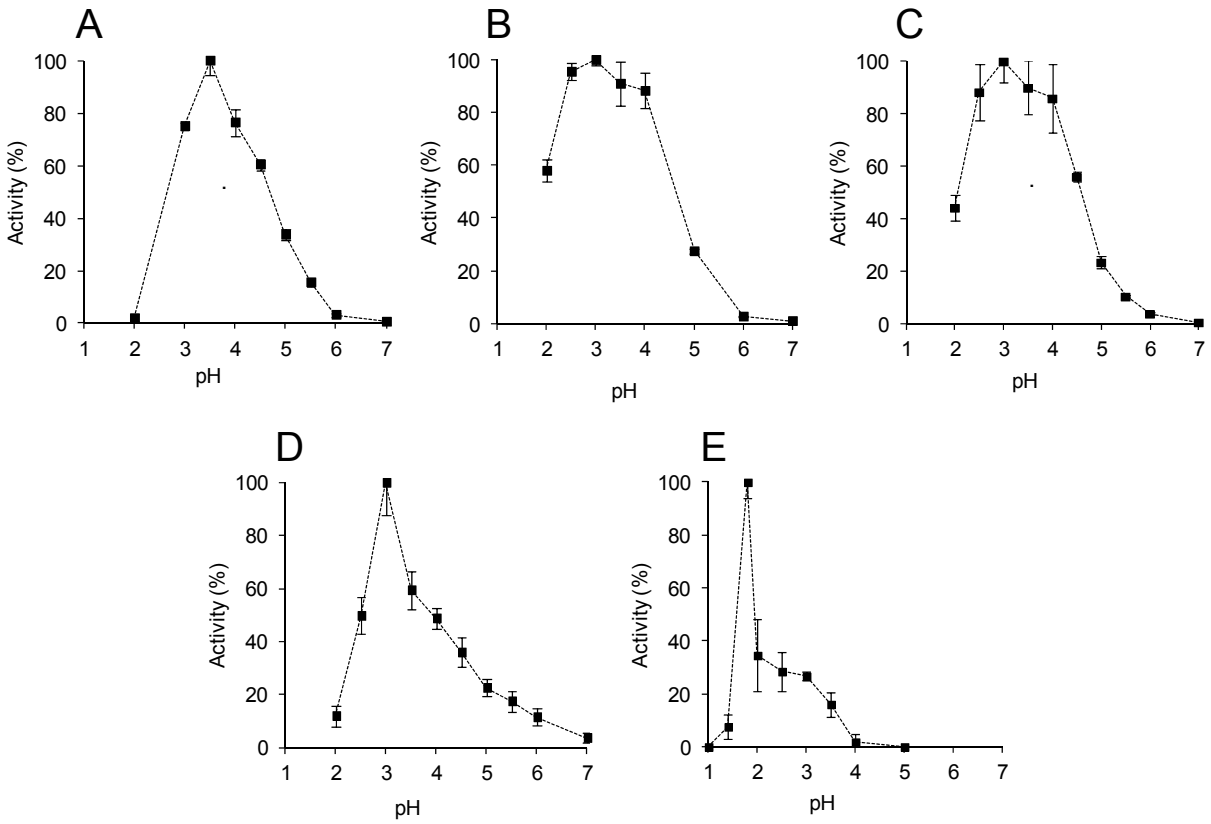

Figure S6 Effect of pH for *A. auricula-judae* DyP oxidation of different substrates

(A-E) Relative activity of recombinant DyP on RB19 (50 µM), DMP (0.5 mM), ABTS (0.5 mM), RB5 (25 µM) and VA (10 mM), respectively, measured in 50 mM Britton-Robinson buffer (pH 2-12) and KCl-HCl (pH 1) buffers. Bars represent the standard deviations of the means of three measurements

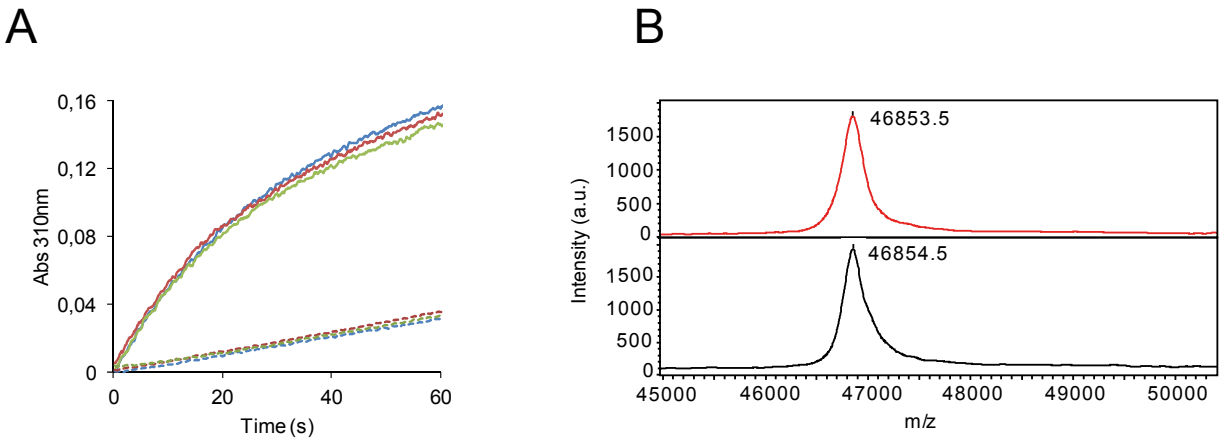

Figure S7 Kinetic and MALDI-TOF evidence for lack of a tyrosine activation mechanism in DyP

(**A**) Absorbance changes at 310 nm (veratraldehyde formation) during oxidation of VA by 10 µM WT DyP (continuous line) and W377S variant (dotted line) previously treated (1 h at 25 ºC) with VA (10 mM) in the presence of 20 µM (red trace) and 100 µM (green trace) H_2O_2, compared with a control incubated with VA alone (blue trace) (reactions in 0.1 M tartrate, pH 2.5, containing 2.5 mM VA, 0.1 mM H_2O_2, and 0.1 mM enzyme). **(B)** MALDI-TOF analysis of the WT DyP (10 µM) treated with 10 mM VA and 0.5 mM H_2O_2 (black profile) compared with an enzyme control incubated without VA and H_2O_2 (red profile). The similar results obtained confirm the absence of a covalent enzyme-VA adduct for activation of a DyP tyrosine residue, as found in *T. cervina* LiP [6].

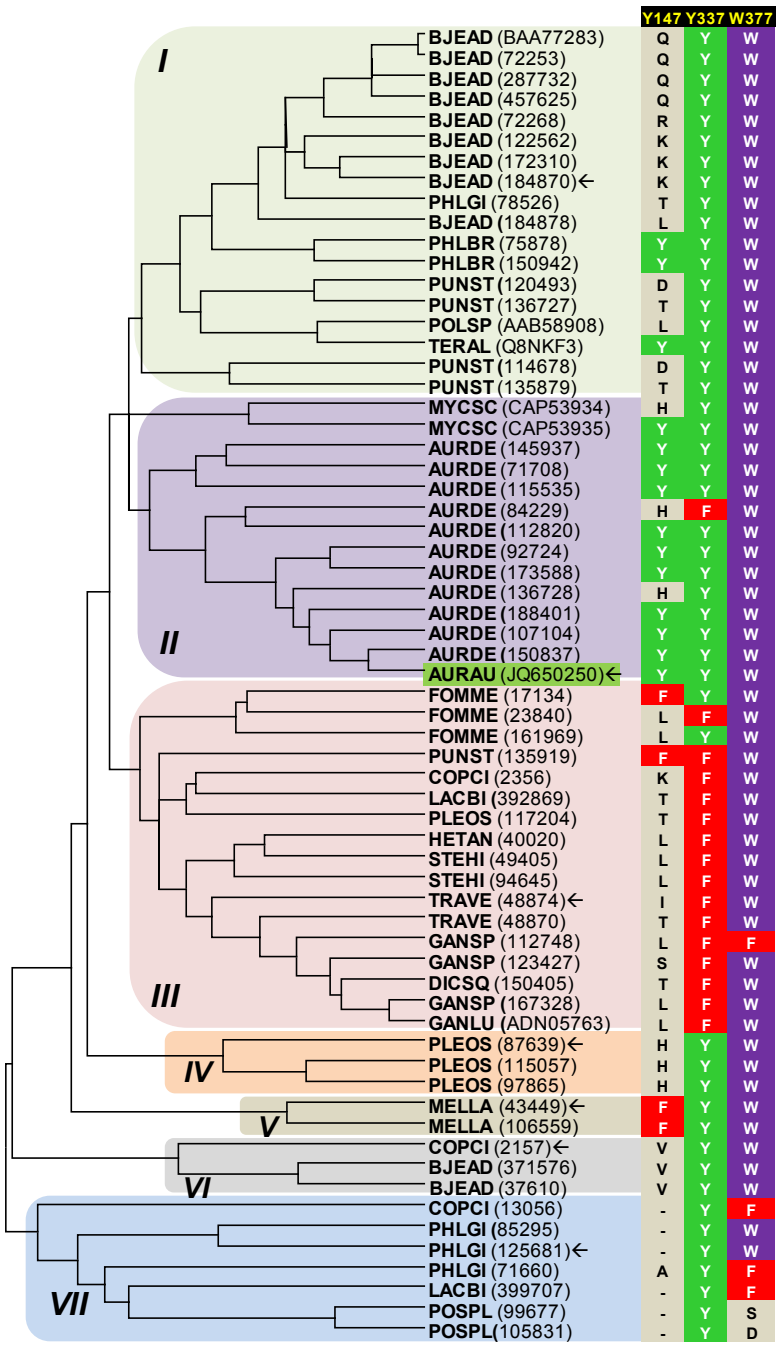

Figure S8 Tyr-147, Tyr-337 and Trp-377 homolog residues in different clusters of basidiomycete DyP phylogram

Sixty-five sequences of basidiomycete DyPs were obtained from the genomes of *Auricularia delicata* (AURAU), *Bjerkandera adusta* (BJEAD), *Coprinopsis cinerea* (COPCI), *Dichomitus squalens* (DICSQ), *Fomitiporia mediterranea* (FOMME), *Ganoderma* sp (GANSP), *Heterobasidion annosum* (HETAN), *Laccaria bicolor* (LACBI), *Melampsora laricis-populina* (MELLA), *Phlebia brevispora* (PHLBR), *Phlebiopsis gigantea* (PHLGI), *Pleurotus ostreatus* (PLEOS), *Postia placenta* (POSPL), *Punctularia strigosozonata* (PUNST), *Stereum hirsutum* (STEHI), and *Trametes versicolor* (TRAVE) available at the JGI (http://genome.jgi.doe.gov) together with GenBank sequences of *A. auricula-judae* (AURAU), *Ganoderma lucidum* (GANLU), *Mycetinis scorodonius* (MYCSC) and *Termitomyces albuminosus* (TERAL). The phylogram obtained with MEGA5 [18] includes three main clusters (I-III and VII; cluster-II containing the *A. auricula-judae* DyP) and three small ones (IV-VI). The JGI and GenBank references are provided, together with indication of the residues occupying the positions homologous to those of *A. auricula-judae* Tyr-147, Tyr-337 and Trp-377 in each of the sequences (details of homology models for the seven DyPs marked with arrows, as representative of the different clusters, are shown in **Fig. S9**).

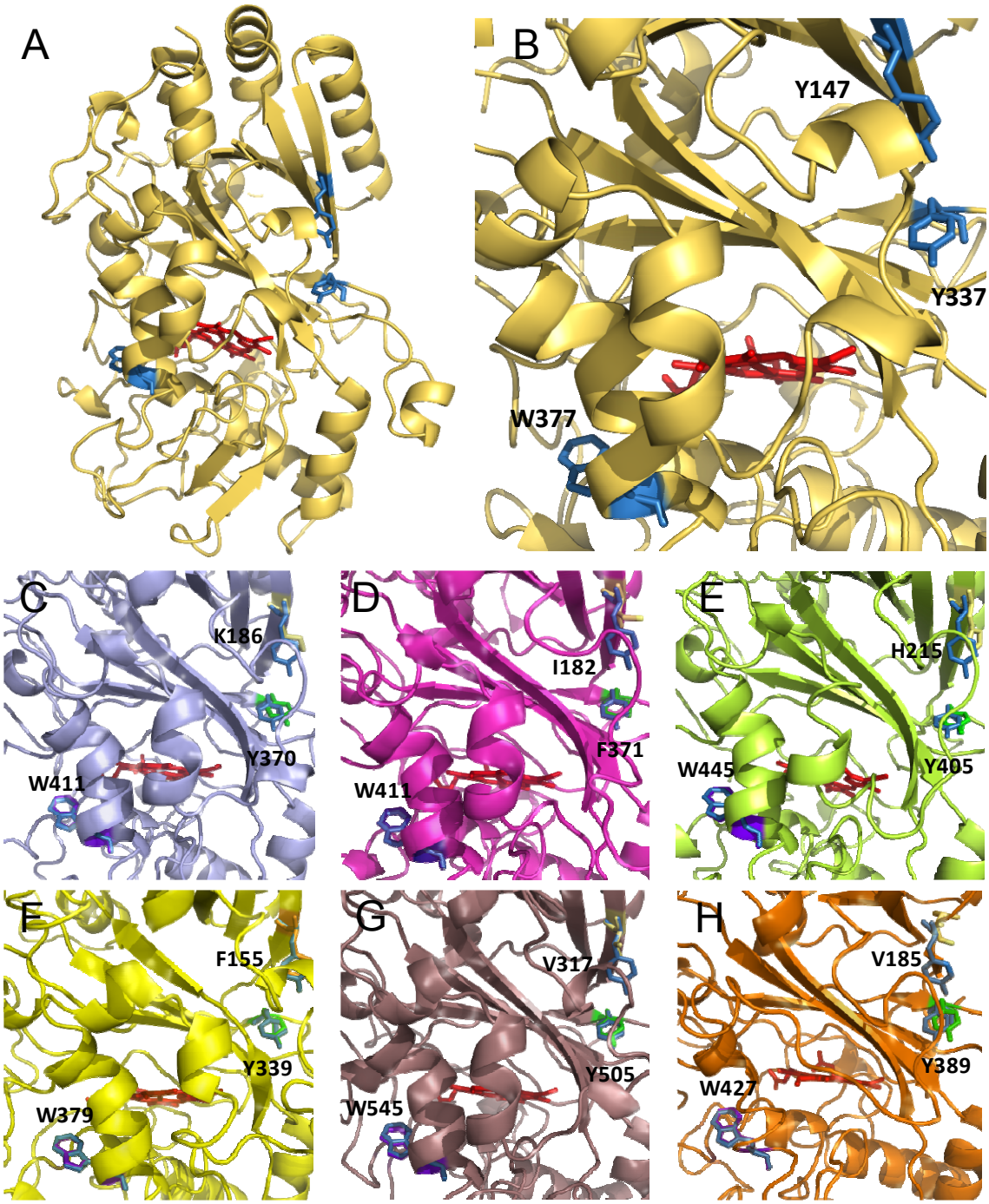

Figure S9 Residues homologous of *A. auricula-judae* DyP Trp147, Tyr337 and Trp377 in basidiomycete DyPs representative for the different clusters of Fig. S8

(A and **B)** Scheme of the whole crystal structure of recombinant *A. auricula-judae* DyP (4W7J) and detail of Tyr-147, Tyr-337 and Trp-377 near the haem cofactor, respectively. **(C-H)** Detail of residues homologous to the above *A. auricula-judae* DyP residues in molecular models for DyPs from the sequenced genomes of *B. adusta* (JGI 184870), *T. versicolor* (JGI 48874), *P. ostreatus* (JGI 87639), *M. laricis-populina* (JGI43449), *C. cinerea* (JGI 2157) and *P. gigantea* (JGI 125681), respectively.

SUPPLEMENTARY MOVIE

Movie S1 PELE trajectory for free substrate diffusion on DyP

One of the 160 free (non-biased) simulations for RB19 diffusion on the DyP molecule provided by PELE software is included, showing substrate binding at the haem access channel and near Trp-377.

REFERENCES FOR SUPPLEMENTARY DATA

1 Kabsch, W. (2010) XDS. Acta Crystallographica Section D-Biological Crystallography, **66,** 125-132

2 Adams, P. D., Afonine, P. V., Bunkoczi, G., Chen, V. B., Davis, I. W., Echols, N., Headd, J. J., Hung, L. W., Kapral, G. J., Grosse-Kunstleve, R. W., Mccoy, A. J., Moriarty, N. W., Oeffner, R., Read, R. J., Richardson, D. C., Richardson, J. S., Terwilliger, T. C. and Zwart, P. H. (2010) PHENIX: a comprehensive Python-based system for macromolecular structure solution. Acta Crystallographica Section D-Biological Crystallography, **66,** 213-221

3 Emsley, P. and Cowtan, K. (2004) Coot: model-building tools for molecular graphics. Acta Crystallogr. D. Biol. Crystallogr., **60,** 2132

4 Davis, I. W., Leaver-Fay, A., Chen, V. B., Block, J. N., Kapral, G. J., Wang, X., Murray, L. W., Arendall III, W. B., Snoeyink, J., Richardson, J. S. and Richardson, D. C. (2007) MolProbity: all-atom contacts and structure validation for proteins and nucleic acids. Nucleic Acids Res., **35,** W375-W385

5 de Lano, W. L. (2002) The PyMOLl molecular graphics system, DeLano Scientific, San Carlos, CA, USA

6 Miki, Y., Pogni, R., Acebes, S., Lucas, F., Fernández-Fueyo, E., Baratto, M. C., Fernández, M. I., de los Ríos, V., Ruiz-Dueñas, F. J., Sinicropi, A., Basosi, R., Hammel, K. E., Guallar, V. and Martínez, A. T. (2013) Formation of a tyrosine adduct involved in lignin degradation by *Trametopsis cervina* lignin peroxidase: A novel peroxidase activation mechanism. Biochem. J., **452,** 575-584

7 Sastry, G. M., Adzhigirey, M., Day, T., Annabhimoju, R. and Sherman, W. (2013) Protein and ligand preparation: parameters, protocols, and influence on virtual screening enrichments. Journal of Computer-Aided Molecular Design, **27,** 221-234

8 Anandakrishnan, R., Aguilar, B. and Onufriev, A. V. (2012) H++3.0: automating pK prediction and the preparation of biomolecular structures for atomistic molecular modeling and simulations. Nucleic Acids Res., **40,** W537-W541

9 Schrödinger. (2011) Jaguar 7.8, LCC, New York

10 Borrelli, K. W., Vitalis, A., Alcantara, R. and Guallar, V. (2005) PELE: Protein energy landscape exploration. A novel Monte Carlo based technique. J. Chem. Theory Comput., **1,** 1304-1311

11 Bowers, K. J., Chow, E., Xu, H., Dror, R. O., Eastwood, M. P., Gregersen, B. A., Klepeis, J. L., Kolossváry, I., Moraes, M. A., Sacerdoti, F. D., Salmon, J. K., Shan, Y. and Shaw, D. E. (2006) Scalable algorithms for molecular dynamics simulations on commodity clusters. Proc. ACM/IEEE Conference on Supercomputing (SC06), Tampa, 11-17 November, 43

12 Schrödinger. (2011) QSite 5.7, LCC, New York

13 Guallar, V. and Wallrapp, F. (2008) Mapping protein electron transfer pathways with QM/MM methods. J. R. Soc. Interface, **5,** S233-S239

14 Sugano, Y., Muramatsu, R., Ichiyanagi, A., Sato, T. and Shoda, M. (2007) DyP, a unique dye-decolorizing peroxidase, represents a novel heme peroxidase family. Asp171 replaces the distal histidine of classical peroxidases. J. Biol. Chem., **282,** 36652-36658

15 Singh, R., Grigg, J. C., Armstrong, Z., Murphy, M. E. P. and Eltis, L. D. (2012) Distal heme pocket residues of B-type dye-decolorizing peroxidase: Arginine but not aspartate is essential for peroxidase activity. J. Biol. Chem., **287,** 10623-10630

16 Pérez-Boada, M., Ruiz-Dueñas, F. J., Pogni, R., Basosi, R., Choinowski, T., Martínez, M. J., Piontek, K. and Martínez, A. T. (2005) Versatile peroxidase oxidation of high redox potential aromatic compounds: Site-directed mutagenesis, spectroscopic and crystallographic investigations of three long-range electron transfer pathways. J. Mol. Biol., **354,** 385-402

17 Martínez, A. T. (2002) Molecular biology and structure-function of lignin-degrading heme peroxidases. Enzyme Microb. Technol., **30,** 425-444

18 Tamura, K., Peterson, D., Peterson, N., Stecher, G., Nei, M. and Kumar, S. (2011) MEGA5: Molecular evolutionary genetics analysis using maximum likelihood, evolutionary distance, and maximum parsimony methods. Mol. Biol. Evol., **28,** 2731-2739